Volume 51
Number 10
14 March 2022
Pages 3765-4184

Dalton Transactions

An international journal of inorganic chemistry

rsc.li/dalton

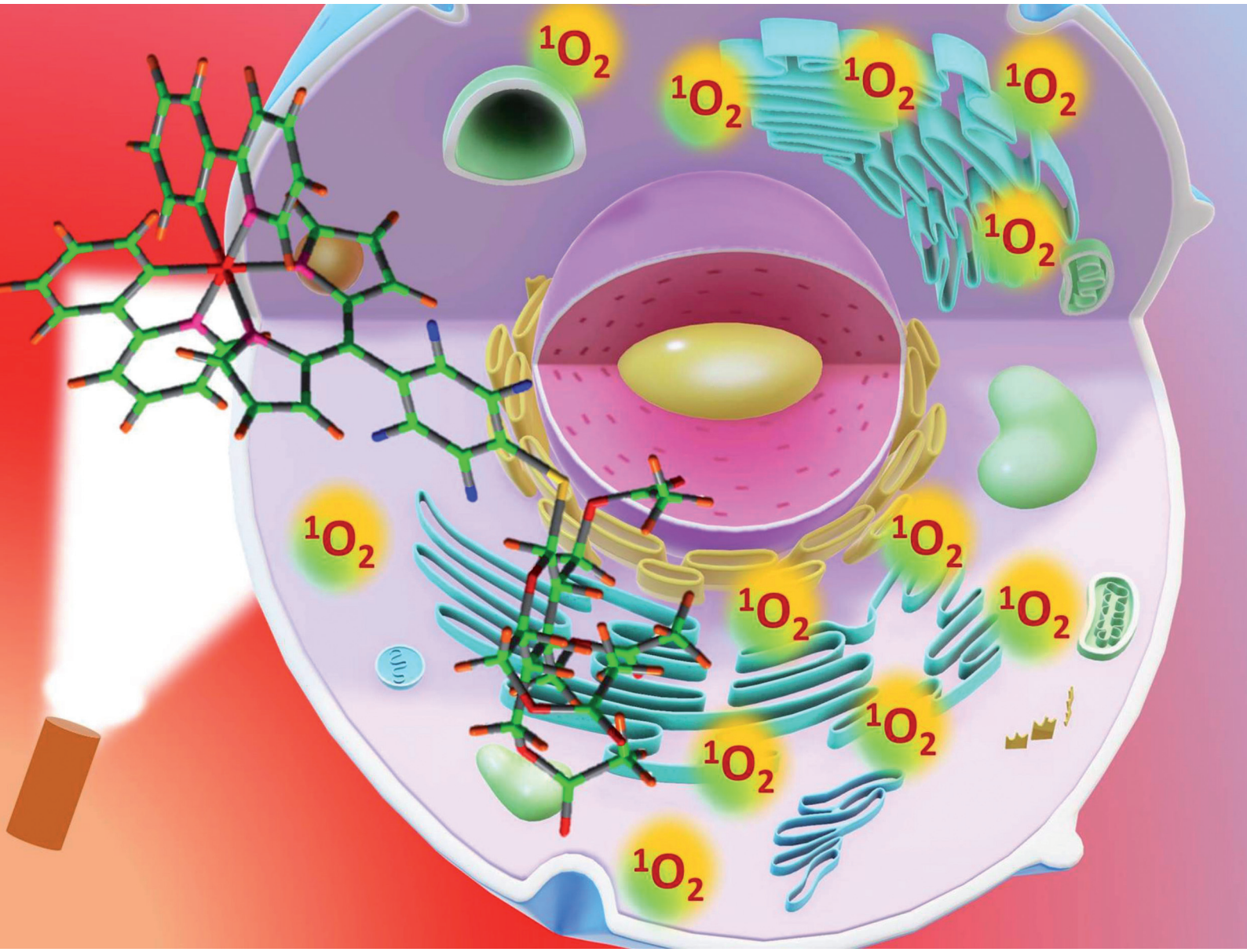

ISSN 1477-9226

ROYAL SOCIETY OF CHEMISTRY

PAPER

Iti Gupta *et al.*

Luminescent iridium(III) dipyrrinato complexes: synthesis, X-ray structures, and DFT and photocytotoxicity studies of glycosylated derivatives

Dalton Transactions

ROYAL SOCIETY OF CHEMISTRY

PAPER

View Article Online
View Journal | View Issue

Cite this: *Dalton Trans.*, 2022, **51**, 3849

Luminescent iridium(III) dipyrrinato complexes: synthesis, X-ray structures, and DFT and photocytotoxicity studies of glycosylated derivatives†

Neha Manav,‡[a] Mohsin Y. Lone,‡[a] Md Kausar Raza,[b] Jaydeepsinh Chavda,[a] Shigeki Mori [c] and Iti Gupta *[a]

Received 15th December 2021,
Accepted 14th February 2022

DOI: 10.1039/d1dt04218a

rsc.li/dalton

A series of luminescent Ir(III) dipyrrinato complexes were synthesized having various aromatic chromophores at the C-5 position of dipyrrin ligands. The presence of different chromophores on the Ir(III) dipyrrinato complexes altered their optical properties and produced strong emission in the red to NIR region (680–900 nm) with huge Stokes shifts (5910–7045 cm^{-1}). TD-DFT studies indicated significant charge distribution between dipyrrin ligands and Ir-cyclometalated units in all the molecules. X-ray crystal structures revealed an octahedral geometry of the Ir(III) center in the complex. The *in vitro* studies of the glycosylated Ir(III) complexes revealed strong photoluminescence with maximum Stokes shifts, and they showed significant photocytotoxicity in skin keratinocyte (HaCaT) and lung adenocarcinoma (A549) cells. The singlet oxygen generation quantum yields of glycosylated Ir(III) complexes were in the range of 70–78% in water. The estimated IC_{50} values were between 17 and 25 μM after light exposure, and confocal microscopy revealed significant localization of the glycosylated Ir(III) complexes in the endoplasmic reticulum (ER) of cancer cells. The neutral Ir(III) dipyrrinato complexes are promising tracking agents for cellular imaging in the biological window and for photodynamic therapy (PDT) applications.

Introduction

The concept of designing metal complexes with fluorescent ligands is a blooming ground of research, especially in chemical biology, as the generated complex derives properties from both the metal source and the fluorescent ligand.[1] Dipyrrins are examples of pyrrole-based ligands in which substituents can be introduced to fine-tune the electronic and spectral properties of the molecules.[2–5] Dipyrrins are widely known for their bidentate chelation with different metal ions[3,6] and the difluoroboron moiety in BODIPYs[7–11] and aza-BODIPYs.[12–15] The dipyrrinato complexes are known for their rich and varied photophysical behaviors and long-lived excited triplet states. The metal dipyrrinato complexes have also received attention for their ability to generate singlet oxygen in the presence of light. The triplet state stability of such metal-based photosensitizers (PSs) governs the singlet oxygen generation activity, which is responsible for cell apoptosis. Phototoxicity offers a much better approach for the treatment of cancer and many photosensitizers based on tetrapyrrolic systems are known in the literature. In spite of their successful clinical trials, their candidature as photodynamic therapy (PDT) drugs is still unsatisfactory. Compared to the applications of organic PSs for phototherapy, metal-based complexes are at an early stage and seek importance because of their high spin–orbit coupling.[16,17]

For better efficacy in PDT, targeting a PS to a subcellular organelle is the need of time. Not only does it help in the nanomolar activity of the PS for PDT but it can also prove to be selective for tumor cells.[18] Certain metal complexes are reported in the literature for enhancing the efficacy of PDT treatment after targeting particular subcellular organelles including the endoplasmic reticulum, cytoplasm, mitochondria, or nucleus.[19] However, accumulation in the mitochondria has been noticed for its comparatively high toxicity in the dark,[20] and the cell nucleus suffered from a high risk of DNA mutation.[21] Therefore, targeting the endoplasmic reticulum

[a]*Indian Institute of Technology Gandhinagar, Palaj Campus, Gandhinagar, Gujarat-382355, India. E-mail: iti@iitgn.ac.in*
[b]*Department of Inorganic and Physical Chemistry, Indian Institute of Science, Bangalore-560012, India*
[c]*Advanced Research Support Center, Ehime University, Matsuyama 790-8577, Japan*

†Electronic supplementary information (ESI) available: Characterization data such as IR, MALDI-MS, ^{1}H, COSY and ^{13}C NMR spectra of iridium complexes. Photophysical studies in different solvents, singlet oxygen studies, the MTT study in the dark and geometry optimization data of metal complexes obtained from DFT calculations. CCDC 2022646 and 2022648. For ESI and crystallographic data in CIF or other electronic format see DOI: 10.1039/d1dt04218a

‡Equal contribution.

(ER) has drawn researchers' attention, and it is considered as an ultimate target that comprises negligible risk and has equivalent efficiency towards cell death by ROS fluctuation. The endoplasmic reticulum (ER) is one of the vital organelles that plays a key role in the synthesis, maturation, folding and export of proteins. Interferences in the signaling pathways of ER redox are the basis of cell demise by ER-stress-induced apoptosis.[22] ER stress increases ROS production which leads to tumor cell death; therefore, ER stress might be effective in the treatment of tumors with minimum possibility of nuclear DNA mutation.[23] ERs are located in close proximity to the nucleus, and thus ER-targeting metal complexes can induce better toxicity by singlet oxygen generation. The predominant localization of the ER-targeting compounds opens up more avenues of exploring such systems because they are known to show higher selectivity towards cancer cells over normal cells.[18] The FDA-approved drugs *bortezomib* and *carfilzomib* are proteasome inhibitors that are successful as ER stress-inducing agents reported in the literature.[18]

Iridium(III) complexes are well known for their rich photophysical properties with a wide application range.[24–26] Their structural variations can be used to alter their reactivity from kinetically labile to inert complexes.[27,28] Such complexes revealed pronounced stability in biological media which prompted the exploration of their photoactivity, although most iridium complexes (with phenyl-pyridine and tetrazolate ligand terpyridyl, *etc.*) explored for ER targeting are cationic and/or neutral complexes.[22,29–32] The neutral Ir(III) complexes generally possess minimal toxicity in the dark compared to charged complexes. Ir(III) cyclometalated complexes are reported to exhibit tunable emission maxima, high luminescent quantum yields and noticeably long phosphorescence lifetimes. Iridium(III) complexes have been used as luminescent probes for biolabeling[33–35] and *in vivo* tumor imaging.[36] In a recent study, Senge and Wiehe[37] reported a wide range of (dipyrrinato)bis(2-phenylpyridyl)iridium(III) complexes along with chlorido(dipyrrinato)(pentamethylcyclopentadienyl) iridium(III) complexes. In this work, the synthesis, crystal structures, and antimicrobial studies of Ir(III) complexes on Gram-positive and Gram-negative microorganisms are discussed. In addition, the anti-cancer and antibacterial activities of glucosyl and galactosyl conjugates of tetrafluorophenyl-substituted and 3-nitrophenyl-substituted dipyrrinato Ir(III) complexes were evaluated in epidermoid and colorectal cancer cells. The glucosyl and galactosyl conjugates of tetrafluorophenyl-substituted Ir(III) complexes showed better phototoxicity as compared to the 3-nitrophenyl-substituted Ir(III) complexes towards tumors and bacteria. The authors reported that the (dipyrrinato) (pentamethylcyclopentadienyl)iridium(III) complexes showed better activity against bacteria even under dark conditions and can be potentially used for antimicrobial applications in the future.[37]

Our aim in this study was to design neutral Ir(III) dipyrrinato complexes linked with other aromatic chromophores. Such hybrid complexes are expected to show strong absorption in the visible region and red to near IR (infrared) emission. Their water-soluble derivatives can be prepared by linking hexose sugars on the dipyrrin ligands for anti-cancer applications. Strong luminescence and large Stokes shifts will be added advantages, which can be utilized for live-cell imaging and PDT applications. In this work, we report a series of Ir(III) dipyrrinato complexes having different *meso*-substituents on dipyrrins, such as *N*-butylcarbazole, benzothiadiazole and pentafluorophenyl groups. These complexes exhibited strong emission in the red to NIR region (680–900 nm) with huge Stokes shifts (5910–7045 cm^{-1}). X-ray crystal structure analysis and TD-DFT studies were performed for better understanding the structure–property relationships of these Ir(III) dipyrrinato complexes. The glucose and galactose conjugated Ir(III) dipyrrinato complexes were prepared and tested for subcellular localization (predominantly in the ER) and as PDT agents for *in vitro* studies in A549 and HaCaT cell lines.

Results and discussion

Synthesis

A cyclometalated iridium complex was prepared as per the reported method.[38] The synthesis of C5-substituted dipyrromethanes was attained by the acid-catalyzed reaction of pyrrole with various aromatic aldehydes.[11,39,40] The substituents at the C5-position of the dipyrromethanes vary from the 2-thienyl, 9-butyl-9*H*-carbazole, 9-butyl-3(thiophen-2-yl)-9*H*-carbazole, pentafluorophenyl and 4-(thiophen-2-yl)benzo[*c*][1,2,5] thiadiazole groups. The different dipyrromethanes were oxidized with DDQ to dipyrromethenes and then reacted *in situ* with cyclometalated iridium complexes in the presence of a base[40–42] to obtain the iridium dipyrrinates **Ir1–Ir5** in 69–81% yields (Scheme 1).

The glycosylated Ir(III) dipyrrinato complexes were synthesized by a nucleophilic substitution reaction of **Ir5**[37] with 2,3,4,6-tetra-*O*-acetyl-β-D-thiagalactopyranose or 2,3,4,6-tetra-*O*-acetyl-β-D-thiaglucopyranose in the presence of a base (Scheme 2). The crude complexes **Ir6** and **Ir7** were purified using alumina column chromatography in 78 and 83% yields, respectively. The water-soluble derivatives **WS-Ir6** and **WS-Ir7** were prepared by the deprotection of acetylated glucose/galactose units by treating **Ir6** and **Ir7** with a base as shown in Scheme 2.

The **Ir8** complex was synthesized from tetramethyl-substituted dipyrromethane (**A**) that was reacted with iodine in the presence of a base to give the oxidized product **B** (Scheme 3). The dipyrrin **B** was further reacted with the cyclometalated iridium complex as shown in Scheme 3 to obtain **Ir8** in good yields (76%). The IR spectra of **Ir1–Ir8** demonstrated vibrational frequencies between 3050 and 550 cm^{-1} and were almost cognate among all the complexes. The C–H stretching vibrational bands of **Ir1–Ir5** were observed at around 2850 to 3020 cm^{-1} which corresponds to the dipyrrin unit and the aryl rings. The ring skeleton C–H bending and C–C stretching vibrations were seen at around 1630 to 1410 cm^{-1}, respectively. The C–N stretching modes of the pyridyl and phenyl groups

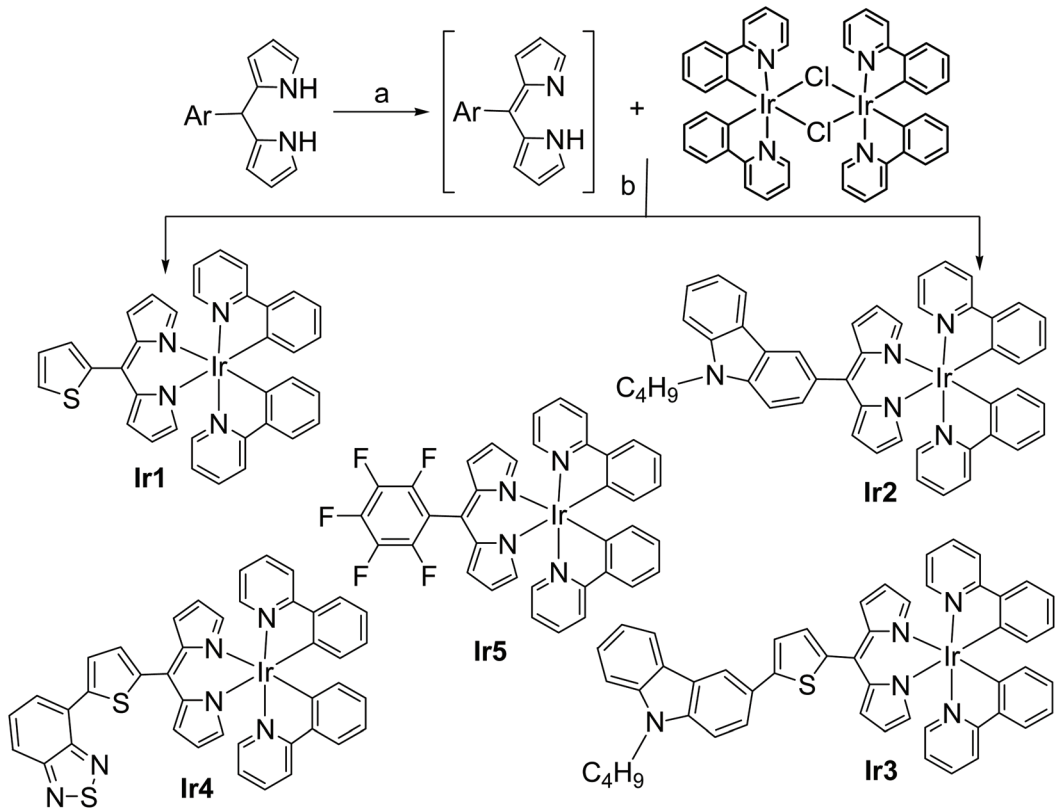

Scheme 1 Synthesis of the Ir(III) dipyrrinato complexes; (a) DDQ, dry THF, 1 h; (b) K_2CO_3, dry THF, 12 h.

were observed between 1374 and 1340 cm^{-1}. The C–H bending (ring) vibrations were observed between 1080 and 1274 cm^{-1} and those of the out of plane modes were observed around 756 to 986 cm^{-1}. The vibrational bands around 705 to 558 cm^{-1} were ascribed to the ring bending that originates from the aryl groups. While **Ir6** and **Ir7** with their acetylated galactose/glucose moieties exhibited characteristic bands for the C=O stretching frequency at 1748 cm^{-1}, the asymmetric C–O–C stretching vibrations were observed at around 1214 cm^{-1}. The water-soluble complexes **WS-Ir6** and **WS-Ir7** displayed a broad IR band at around 3352 cm^{-1} corresponding to the –OH groups, clearly indicating that the deprotection of the acetyl groups was achieved. A molecular ion peak in the MALDI-mass analysis also confirmed the formation of **WS-Ir6** and **WS-Ir7** (ESI†).

The NMR spectra of complexes **Ir1–Ir8** and the precursor dipyrromethenes were recorded in CD_2Cl_2 and $CDCl_3$, respectively (ESI†). A representative ^{1}H-NMR and partial COSY spectra of **Ir2** are shown in Fig. S7 (ESI†). The characteristic six pyrrole protons of the dipyrrin unit showed up as three sets of multiplets at 6.22, 6.57 and 6.84 ppm and the seven protons of the carbazole ring appeared between 8.19 to 7.22 ppm. The aromatic protons of the pyridyl and phenyl rings showed up as multiplets between 7.91 to 6.43 ppm (Fig. S7†) and the nine alkyl protons appeared as four sets of signals between 4.39 to 0.99 ppm.

The ^{19}F NMR spectra of **Ir5–Ir8** were recorded in CD_2Cl_2 at room temperature (ESI, Fig. S20, S25, S30 and S35†). Due to the substitution of one fluorine atom of the pentafluorophenyl ring by the thioglycosyl group, the ^{19}F NMR spectra showed two signals corresponding to four F atoms between −132 and −140 ppm. This pattern reflected the substitution of the C_5F_5 ring in the **Ir6** and **Ir7** complexes, whereas unsubstituted **Ir5** revealed three signals at −140, −154, and −162 ppm in the ^{19}F NMR spectrum. A similar pattern was also observed in the ^{19}F NMR spectrum of **Ir8** with three signals at −140, −153, and −162 ppm.

X-ray crystal structures

The molecular structures of **Ir1** (CCDC 2022646†) and **Ir4** (CCDC 2022648†) were further confirmed by single-crystal X-ray analysis; the Ortep diagrams are shown in Fig. 1 and 2, respectively. Block crystals of **Ir1** (black) and **Ir4** (red) suitable for crystallography measurements were obtained by the slow evaporation of a chloroform/pentane solution for two weeks. The crystal sizes of **Ir1** and **Ir4** observed were 0.4 × 0.8 × 0.10 mm and 0.13 × 0.10 × 0.15 mm, respectively. The crystallographic data and the selected bond lengths and bond angles are arranged in Tables S1 and S2,† respectively. The Ir(III) metal center has an octahedral geometry as evident from the X-ray structures shown in the Ortep diagrams.

From Table S2,† it is evident that the torsion angles [C26–C27–C32–S1 and C28–C27–C32–C33] of **Ir4** (with thiophene as the linker between the dipyrrin unit and benzothiadiazole) were significantly higher than those of **Ir1** (the 2-thienyl group

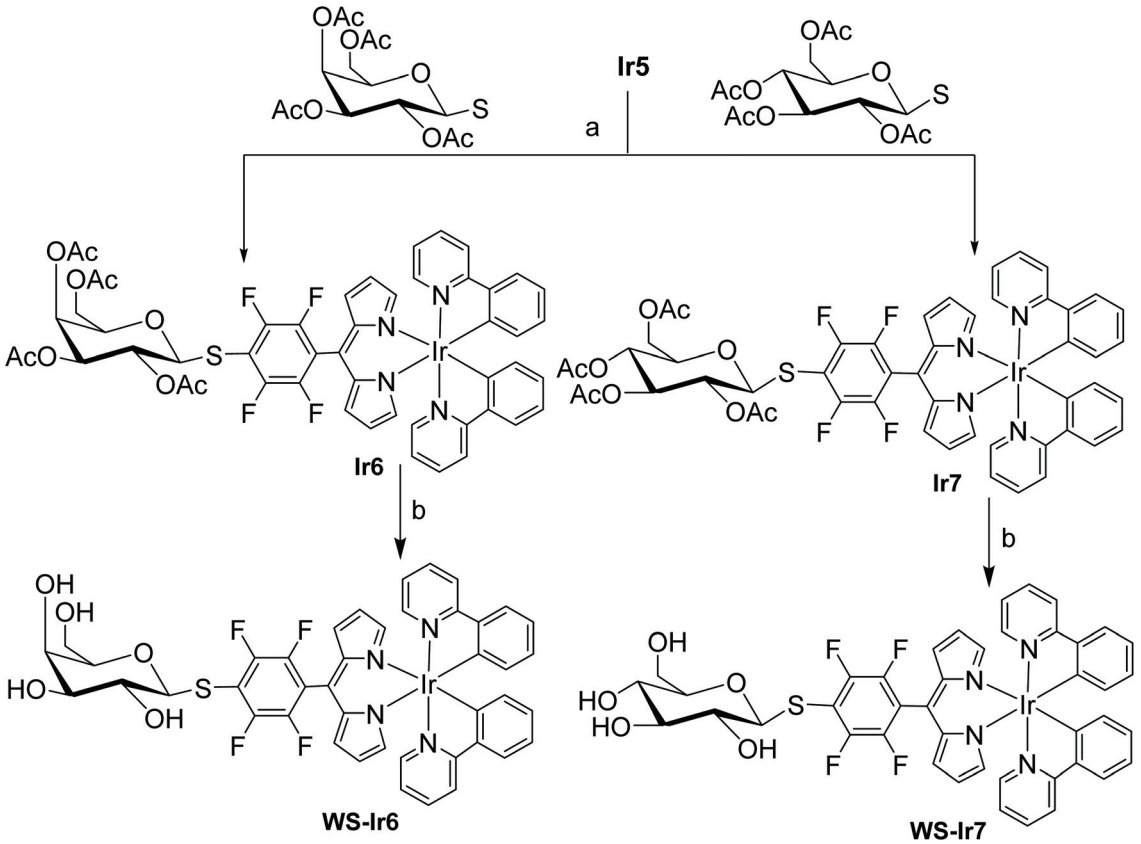

Scheme 2 Synthesis of the glycosylated Ir(III) dipyrrinato complexes, (a) dry DEA, dry DMF, 12 h; (b) NaOMe/MeOH, 3 h.

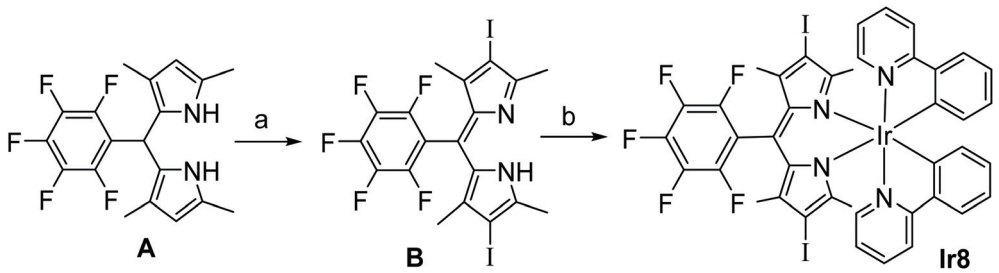

Scheme 3 Synthesis of the **Ir8** complex; (a) I_2, K_2CO_3, methanol, 12 h and (b) cyclometalated iridium complex, K_2CO_3, dry THF, 12 h.

at the dipyrrin ring). The observed bond distances between the iridium atom and two nitrogens (Ir–N3 and Ir–N4) of the dipyrrin unit were 2.126(3) and 2.127(3) for **Ir1** and 2.115(7) and 2.142(7) for **Ir4**. In addition, the distance between phenyl pyridine and the iridium atom [Ir–N1, Ir–N2, Ir–C7, and Ir–C18] for both **Ir1** and **Ir4** were observed to be nearly in the same range [~2.04, ~2.04, ~2.02, and ~2.01 Å]. The bond distances and bond angles observed in the DFT optimized geometries of **Ir1** and **Ir4** are also provided in Table S2;† the X-ray structural data match closely with the DFT optimized molecular structures.

Absorption studies

The absorption and emission spectra of the iridium dipyrrinato complexes **Ir1–Ir8** were measured in different solvents like toluene, DMSO, THF, hexane, *etc*. ranging from low polarity to high polarity (ESI†). The absorption and emission data of complexes **Ir1–Ir8** in DMSO and toluene are presented in Table 1.

The complexes **Ir1–Ir7** showed mainly two absorption bands; the major absorption band with the maxima ranging from 478 nm to 500 nm in DMSO (Fig. 3) and in toluene (Fig. S50a†) that were attributed to the π to π* transitions of the dipyrrinato ligand. Such an absorption pattern is similar to those of the reported metal dipyrrinato complexes,[39,43] where ligand-centric transitions are dominant and the maxima are not influenced much by the insertion of metal or by the different substituents on the dipyrrinato ligand. However, the absorption bands were slightly narrow as compared to those of

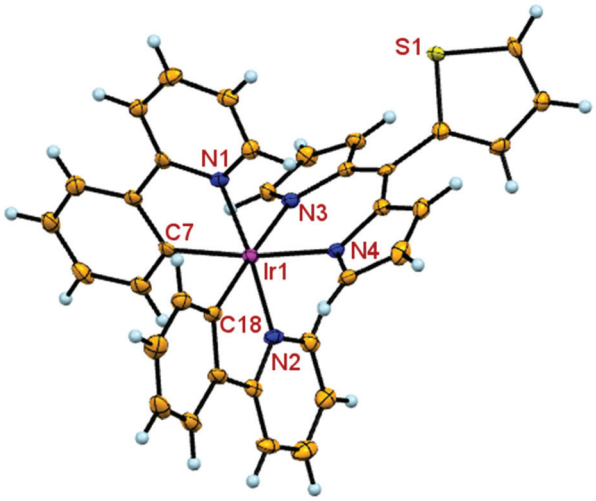

Fig. 1 ORTEP diagram of **Ir1** and thermal ellipsoids are shown at 50% probability level.

the free dipyrrin ligand. In the case of complex **Ir8**, the intense absorption band lays around 536 nm with a high molar extinction coefficient (Table 1). This transition is akin to the π to π* transition but is 40–51 nm red-shifted than those of the other Ir(III) dipyrrinato complexes; the presence of two α-methyl groups on the dipyrrin ligand could be the reason for such a bathochromic shift in the **Ir8** complex. The complexes **Ir2–Ir4** also possess a shoulder band at around 400–430 nm, which could be assigned to the MLCT transitions. The complexes **Ir1–Ir8** exhibited another weak intensity band at ~350 nm that can be attributed to the ligand-centric ICT (intra-molecular charge transfer) transitions.[41] Among the eight complexes, **Ir2**, **Ir3** and **Ir4** showed higher absorption coefficients than the other compounds, suggesting that the substitution of the carbazole and benzothiadiazole groups on the dipyrrin core affected their electronic properties. The major absorption bands of complexes **Ir1–Ir7** showed a 10–14 nm red shift and the complex **Ir8** revealed a ~52 nm red shift with respect to the absorption wavelength (484 nm in toluene)[44] of the parent Ir-cyclometalated complex having a phenyldipyrrin ligand.[44] To further explore the solvatochromic behavior of the complexes **Ir1–Ir8**, their absorption spectra were recorded in various solvents and the data are provided in the ESI† (Fig. S51†). The study revealed that the polarity of solvents does not have a significant effect on the absorption maxima of the complexes; but for few compounds, ~10 nm shifts were observed in polar solvents. For example, the wavelength of the major absorption band of **Ir1** was shifted from 489 nm to 497 nm upon changing the solvent from acetonitrile to CCl_4. Other complexes also showed 8 to 10 nm red shifts in their absorption maxima in polar solvents.

Luminescence study

Organometallic complexes of heavy metals like Pd(II), Pt(II), Re(I), and Ir(III) are known for their phosphorescent properties and have some advantages over pure organic fluorophores, such as the long triplet state lifetime due to the ISC and large Stokes shifts. The photoluminescence (PL) spectra of **Ir1–Ir8** were recorded at room temperature in deoxygenated solvents and the data are given in Table 1. A comparison of the photoluminescence spectra of **Ir1–Ir8** is presented in Fig. 4 and the emission spectra recorded in toluene are provided in Fig. S50 (ESI†). The Ir(III) complexes showed vibronically structured luminescence with the emission maxima in the range of 678–827 nm in toluene (Table 1). Typically, the Ir-cyclometalated complexes emit at a similar wavelength; a small variation in emission maxima was found when the substituents were changed on the ancillary ligands.

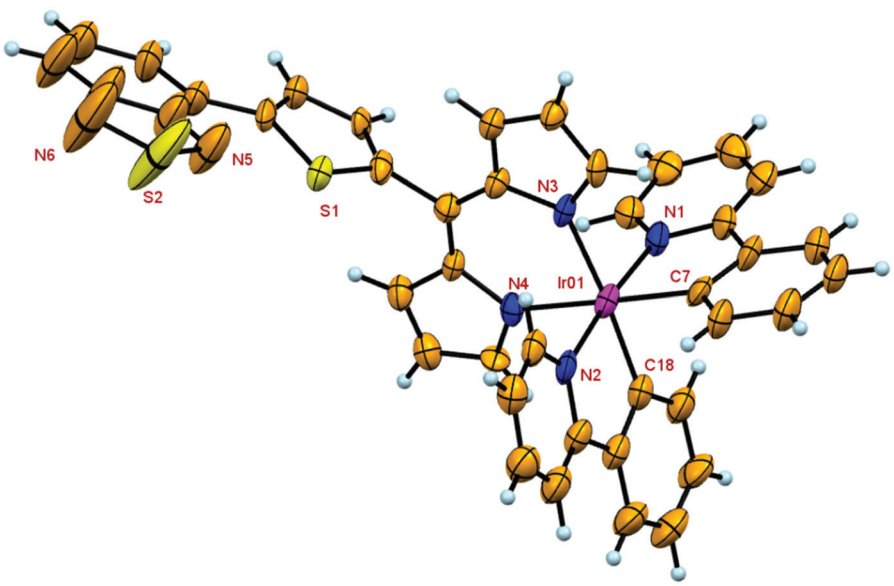

Fig. 2 ORTEP diagram of **Ir4** and thermal ellipsoids are shown at 50% probability level.

Table 1 Absorption and emission data of Ir(III) complexes. The concentration used was (2.4×10^{-6} M)

Complex	Solvent	λ_{abs} (nm)	Log ε	λ_{em} (nm)	Stokes shift (cm^{-1})
Ir1	Toluene	495, 354	4.73	713, 779	6177
	DMSO	494, 347	4.36	717, 778	6296
Ir2	Toluene	484, 407, 336	4.84	678, 737	5912
	DMSO	483, 401, 345	4.54	682, 738	6041
Ir3	Toluene	496, 442 (sh)	4.86	714, 779	6156
	DMSO	495, 442 (sh)	4.57	725, 778	6409
Ir4	Toluene	498, 434	4.79	722, 791	6230
	DMSO	497, 407	4.36	725, 789	6328
Ir5	Toluene	494	4.86	737, 799	6674
	DMSO	492	4.47	740, 795	6812
Ir6	Toluene	494	4.75	747, 800	6856
	DMSO	492	4.52	753, 792	7045
Ir7	Toluene	494	5.82	747, 800	6856
	DMSO	492	4.47	753, 792	7045
Ir8	Toluene	536	5.03	827	6565
	DMSO	535	4.69	823	6541

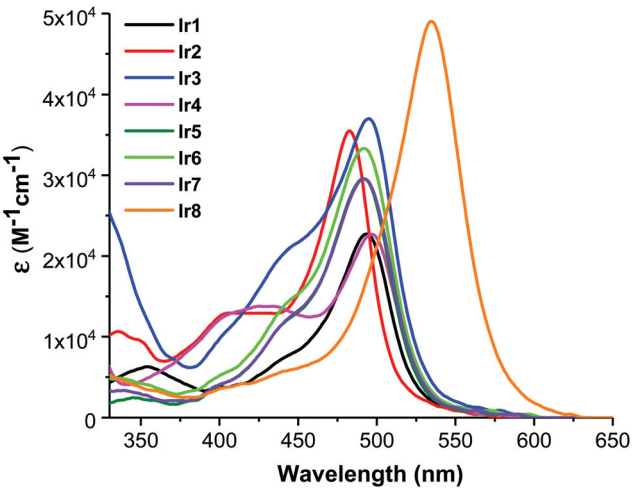

Fig. 3 Absorption spectra of the Ir(III) dipyrrinato complexes in DMSO.

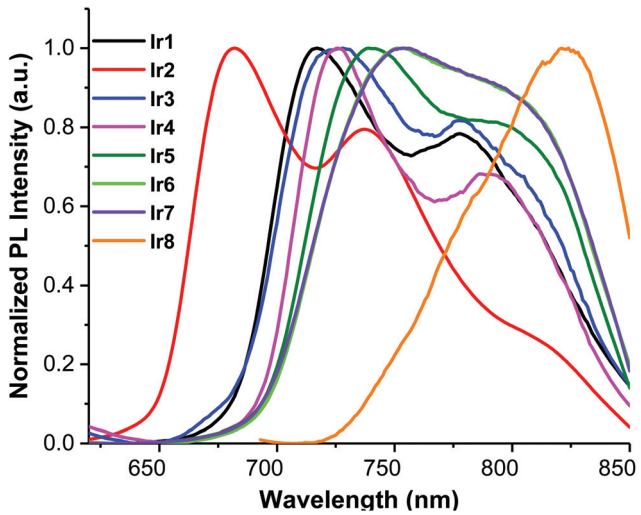

Fig. 4 Luminescence spectra of the Ir(III) complexes in DMSO (λ_{ex} = 485 nm).

The major emission band observed for Ir(III) complexes is mainly ligand centric in nature, with dominant contributions from the ^{3}LC (π–π^*) and MLCT (dπ–π^*) transitions. The emission wavelengths were significantly affected by the change of *meso*-substituents on the dipyrrinato ligand, suggesting that the emission originates from the dipyrrin unit. The presence of heavy metal Ir is responsible for the increased ISC in the complexes, which resulted in the $^3(\pi$–$\pi^*)$ state being localized in the dipyrrin unit. As compared to the luminescence of the parent Ir-bis-cyclometalated complex having a *meso*-phenyl dipyrrin (λ_{em} = 691 nm, toluene),[44] the emission maxima of **Ir1**–**Ir8** were considerably red-shifted. Concerning the emission of the parent Ir(III) complex, **Ir1**/**Ir3** and **Ir4** showed ~23 nm and ~31 nm bathochromic shifts, respectively. Whereas, **Ir5**–**Ir7** exhibited 46–56 nm red-shifted emission maxima as compared to the parent Ir(III) complex. The presence of two iodine atoms on the dipyrrin ligand in **Ir8** caused a large red shift of 135 nm in the emission band as compared to the parent compound. The solvatochromic emission behavior was less evident in the **Ir1** and **Ir2** complexes. While, in hexane, the emission maxima of **Ir1** and **Ir2** were observed at 711 and 675 nm, respectively, the emission maxima of **Ir1** and **Ir2** in DMF were shifted to 717 and 681 nm, respectively. Similarly, other iridium complexes also showed 6–7 nm red shifts in the emission maxima while moving from less to more polar solvents (Fig. S52, S53†). All the complexes exhibited huge Stokes shifts in the range of 5910 to 7045 cm^{-1}; particularly, **Ir6** and **Ir7** with galactose and glucose units on dipyrrin ligands showed relatively larger Stokes shifts as compared to the rest of the compounds (Table 1).

DFT studies

The complementary spectroscopic insight into the roots of the absorption bands of **Ir1**–**Ir8** was offered by calculating the singlet–singlet electronic transitions, employing the PCM-TD-B3LYP/6-31+(d)//PCM-B3LYP/6-31G(d) level of approximation. The effect of DMSO was considered, owing to the insignificant effect of other solvents on the absorption profiles of these complexes. Prior to the comparison of the lowest energy transitions (λ_{max}) of the **Ir1**–**Ir8** complexes, the nature of the transitions was examined. To accomplish this, the topologies of the molecular orbitals accountable for the transitions were determined. The calculated frontier molecular orbitals (FMOs) and the absorption maxima along with their oscillatory strengths (f) are listed in Fig. 5 and Table S3,† respectively. The geometry optimized structures are well correlated with the X-ray crystallographic data. The calculated bond lengths (Ir–N1 to Ir–N4) and bond angles (N1–Ir–C1 to N3–Ir–N4) are within 0.07 Å and/or 2° deviation from the structures obtained from X-ray crystallography (Table S2†). It is apparent from the DFT results that the most intense singlet–singlet transitions ($S_0 \rightarrow S_1$) of the molecules **Ir1**, **Ir2**, **Ir5**, **Ir6** and **Ir7** are due to the electron promotion principally from the HOMO−1 → LUMO along with the other transitions mentioned in Table S3.† Notably, for **Ir1**, **Ir2**, **Ir5**, **Ir6** and **Ir7**, the HOMO−1 → LUMO transition is a $\pi \rightarrow \pi^*$ transition of the substituted dipyrromethene

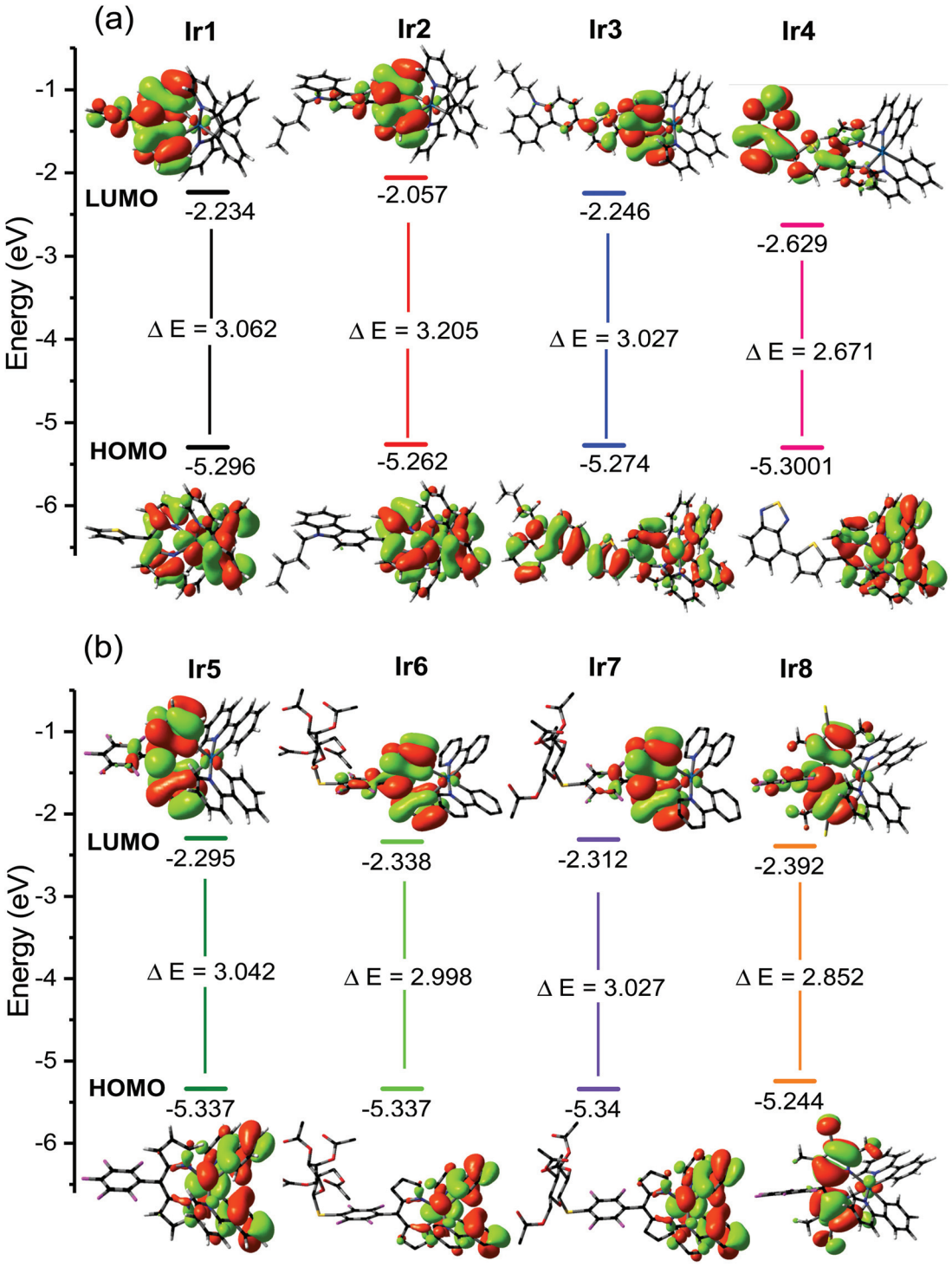

Fig. 5 DFT calculated frontier orbitals and the HOMO/LUMO energies of (a) **Ir1–Ir4** and (b) of **Ir5–Ir8**.

ligand along with the inter-ligand charge transfer. Similarly, the intense singlet–singlet transitions ($S_0 \rightarrow S_1$) of the molecules **Ir3**, **Ir4** and **Ir8** are predominantly due to the HOMO−2 → LUMO, HOMO−1 → LUMO+1 and HOMO → LUMO transitions, respectively, along with the other transitions tabulated in Table S3.†

Akin to previous complexes, these transitions are also dominant $\pi \rightarrow \pi^*$ transitions occurring in the substituted dipyrromethene ligand. However, the intense singlet–singlet transition in **Ir4** is due to the $\pi \rightarrow \pi^*$ transition accompanied by the inter-ligand charge transfer towards the benzothiadiazole moiety. Overall, all the significant transitions of the complexes

under investigation were of $\pi \rightarrow \pi^*$ and inter-ligand charge transfer characteristics. In general, several absorption bands were seen in the calculated spectra of the complexes **Ir1–Ir8**; however, only λ_{max} was chosen for comparison. The calculated and observed λ_{max} values of **Ir1–Ir8** are listed in Table S3.† A significantly good agreement between the calculated and observed λ_{max} values was seen for all the complexes of interest. In particular, the maximum deviation of 95 nm was shown by **Ir4**, followed by **Ir5** and **Ir7** both of which displayed the difference of 94 nm and 93 nm, respectively. It is imperative to mention that all the molecules were consistently underestimated, owing to the inherent limitations of vertical approximation. Moreover, the minor effect of various substituents at the C5 position of the dipyrrin ligand was reflected from the shifts in the λ_{max} values of **Ir1–Ir7**. However, the presence of electron-donating methyl and electron-withdrawing iodine substituents on the dipyrrin ligand in **Ir8** has resulted in a significant red shift in λ_{max}. These observations were in correspondence with the experimental results.

For **Ir1–Ir8**, the spin density contours are localized on the Ir-cyclometalated ligand in the HOMOs and very little or no electron density is observed on the dipyrrin unit. In contrast, in the case of LUMOs, the spin density is mainly localized on the dipyrrin ligand (Fig. 5), indicating inter-ligand CT in the Ir(III) dipyrrinato complexes. The DFT approach was also exploited to calculate the energies of the FMOs and the HOMO–LUMO energy gap (ΔE). As shown in Fig. 5, the energy level of the HOMO and LUMO was centered around −5.3 eV and −2.2 eV, respectively. To be more precise, the utmost difference in the energy level of the HOMO and LUMO was found to be 0.10 eV and 0.33 eV, respectively, as we moved from **Ir1** to **Ir8**. Consequently, the least HOMO–LUMO energy gap was observed for **Ir4** followed by **Ir8** and **Ir6**. Interestingly, **Ir3** and **Ir7** displayed equal HOMO–LUMO energy gaps, whereas **Ir5** and **Ir1** were on the upper side with **Ir2** at the top.

Singlet oxygen studies

The generation of singlet oxygen after light irradiation of the photosensitizer is essential for the photodynamic therapy of cancerous cells. Singlet oxygen ($^1O_2$) is a highly reactive species that is responsible for cancerous cell cytotoxicity. The type of photochemical reaction (type I and type II) is one of the methods to determine the type of ROS generation. The type II mechanism is mainly accountable for the generation of $^1O_2$, which is the dominant cytotoxic species in PDT studies of different photosensitizers.[30,45–48] To quantify the singlet oxygen quantum yields of the iridium complexes **Ir5–Ir7**, the modified literature method was used.[30,48,4950]

The singlet oxygen generation was examined in DMSO, water and $CHCl_3$ saturated with oxygen. DPBF was used as the scavenger with iridium complex using Rose Bengal as the reference compound. The experimental details are provided in the ESI†. The singlet oxygen study of **Ir7** was carried out in DMSO (Fig. 6) using Rose Bengal as the standard.[46] The decrease in the intensity of DPBF of ~420 nm (Fig. 6a and c) was monitored through a UV-vis spectrometer. The complex **Ir7** revealed 50% singlet oxygen quantum yield in DMSO solvent. The plots of singlet oxygen studies for iridium complexes **Ir5**, **Ir6**, and **Ir7** in DMSO, $CHCl_3$ and water are provided in the ESI (Fig. S45–S49 and S61†) and the values are summarized in Table 2. The water-soluble derivatives of the glycosylated Ir(III) dipyrrinato complexes **WS-6** and **WS-7** were also tested for singlet oxygen generation and the data are provided in Table 2. The obtained values of singlet oxygen quantum yield varied from 70% to 78% (in water) suggesting that the iridium complexes can be used as effective photosensitizers in PDT.

Photocytotoxicity and cellular imaging

The cationic iridium(III) cyclometalated complexes have been used for bioimaging applications owing to their good solubility in polar solvents. The large Stokes shifts originating from phosphorescent dyes and their tunable emission wavelengths with moderate quantum efficiencies are added advantages for their biological applications.[32,51,52] The strong absorption in the visible range and phosphorescence in the red to NIR region prompted us to test the neutral Ir(III) dipyrrinato complexes for biological studies.[53] The cell viability studies were carried out for **Ir6** and **Ir7** (having acetyl-thiogalactose and acetyl-thioglucose groups on the dipyrrin ligand). In addition, the free ligand having the pentafluorophenyl group (**L5**) was tested for studying the effect of iridium metalation. The MTT assay was performed on the skin (HaCaT) and lung (A549) cancer cell lines to test the influence of **Ir6**, **Ir7** and the free ligand (**L5**) on cell proliferation. The calculated IC_{50} values of **Ir6** and **Ir7** in HaCaT cells (dark conditions) were around 82 μM (Fig. S54a† and Table 3). Whereas after light exposure, the IC_{50} values were changed to 21.2 and 17.6 μM for **Ir6** and **Ir7**, respectively (Fig. 7, S62† and Table 3). Likewise, the IC_{50} values were calculated for the A549 cell line both in the dark and light; under the dark conditions, the values were between 88.5 and 84.3 μM for **Ir6** and **Ir7** (Fig. S54b† and Table 3). In the presence of light, the calculated IC_{50} values were between 25.5 and 17.8 μM (Fig. 7, S62† and Table 3) for the Ir(III) dipyrrinato complexes. The MTT assay was also performed for the water-soluble derivatives of Ir(III) dipyrrinato complexes, **WS-Ir6** and **WS-Ir7** (ESI, S63†). After 24 h of incubation of **WS-Ir6** and **WS-Ir7** with A549 cancer cells, the cytotoxicity values were 20–40% under light and 40–50% under dark conditions, respectively (ESI, S63†).

The observed IC_{50} values were significantly lower in the presence of light than under dark conditions, reflecting the effective phototoxicity of the photosensitizers **Ir6** and **Ir7** in HaCaT and A549 cancer cell lines. The iridium dipyrrinate **Ir7** (with the glucose moiety) exhibited lower IC_{50} values than its galactose analog **Ir6** (Table 3); the high photocytotoxicity can probably be related to the higher uptake of **Ir7** by the cancer cells. The phototoxicity index (PI) showed that the photosensitizers are ~4 times more active under light than under dark conditions; this could be related to their singlet oxygen generation ability in the cancer cells. Transition metal complexes of Ir, Pt, Pd, Ru, *etc.* are known to generate ROS (reactive oxygen species) both by type I and type II pathways in cancer cells,[18]

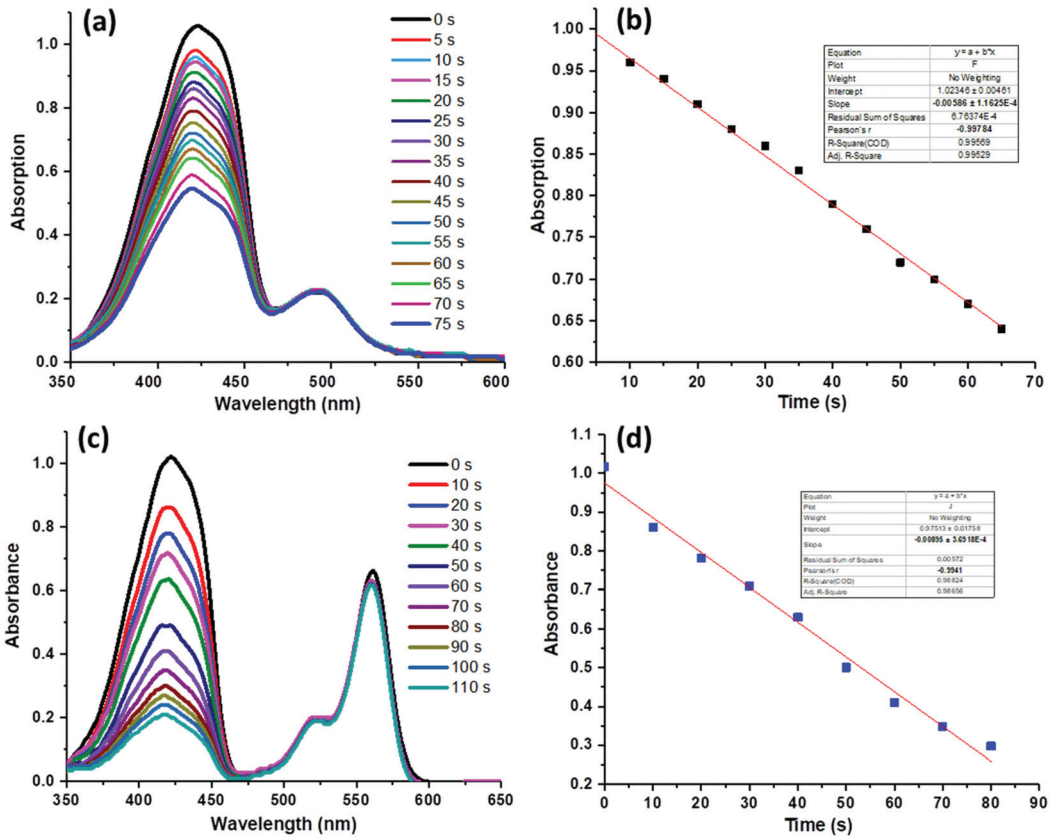

Fig. 6 UV-vis spectral changes in DMSO upon photoirradiation of (a) **Ir7** (λ = 488 nm, 15 mW) and (c) Rose Bengal (λ = 532 nm, 15 mW); the gradual decrease in absorption measured at 420 nm represented in (b) **Ir7**, and (d) Rose Bengal. The concentration used for DPBF was 60 μM; **Ir7** (8 μM) and Rose Bengal (8 μM).

Table 2 Singlet oxygen quantum yields of Ir(III) dipyrrinato complexes with Rose Bengal as the reference

Complex	DMSO, Φ_Δ	$CHCl_3$, Φ_Δ	Water, Φ_Δ
Ir5	63%	93%	—
Ir6	11%	82%	70%
Ir7	10%	86%	76%
WS-6	—	—	74%
WS-7	—	—	78%

Table 3 IC_{50} values of **Ir6** and **Ir7** along with the ligand **L5** after 24 h incubation in HaCaT and A549 cells

	Cell line	**Ir6**	**Ir7**	Ligand
Dark	HaCaT	82.1 ± 1.6	81.8 ± 1.4	>100
	A549	88.5 ± 1.1	84.3 ± 1.9	>100
Light	HaCaT	21.2 ± 0.5	17.6 ± 0.8	78.7 ± 1.9
	A549	25.5 ± 0.3	17.8 ± 0.5	77.9 ± 1.2

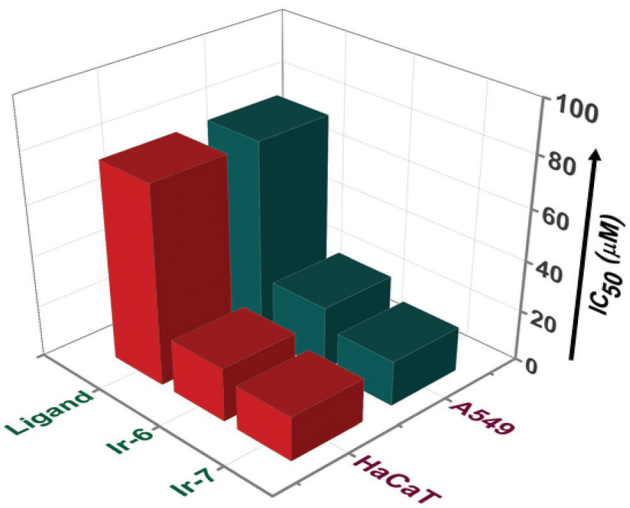

Fig. 7 IC_{50} values in the presence of light; the HaCaT and A549 cell lines were treated with the iridium dipyrrinates **Ir6** and **Ir7** and the ligand (**L5**) after 24 h incubation, was exposed to light (λ = 400–700 nm, 10 J cm^{-2} for 1 h).

making them useful PSs for PDT and photochemotherapy (PCT). Cyclometalated polypyridyl complexes of Ir(III) are reported to be highly luminescent and tend to localize to the ER; ROS generation after light irradiation damages the ER, causing cell apoptosis.[29,30] The role of metal in causing ER stress is evident from the data in Table 3; the free ligand (**L5**) showed IC_{50} values around 78 μM in cancer cells after light exposure (Fig. 7). On the other hand, the calculated IC_{50} values

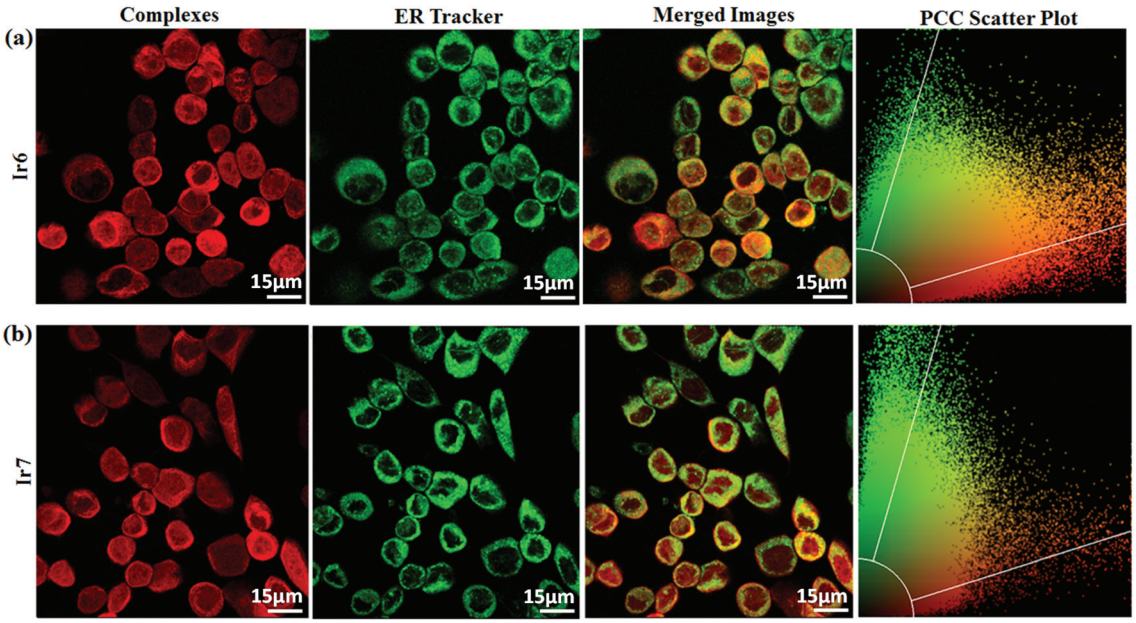

Fig. 8 Confocal microscopic images of (a) **Ir6** (top) and (b) **Ir7** (bottom) showing red emission in the HaCaT cell line after 24-hour incubation in the dark; merged panels with the ER tracker showing endoplasmic reticulum localization of iridium dipyrrinates. Scale bar 15 μm.

were not impressive in the dark (Table 3) for the free ligand (**L5**).

The large Stokes shifts of the iridium dipyrrinato complexes (5910–7045 cm^{-1}) are advantageous for bio-imaging applications as they allow easy detection of the dyes in biological tissues and reduce the effect of autofluorescence. Confocal microscopy was used to investigate the luminescent imaging of **Ir6** and **Ir7** in HaCaT cells (Fig. S64†). The confocal overlaid images of contrast were taken after 24 h incubation of **Ir6** and **Ir7** using DAPI (a nucleus staining dye) as shown in Fig. S64.† It is evident from the merged images that **Ir6** and **Ir7** exhibit cytoplasmic distribution in HaCaT cells (Fig. S64†).

The ER stress is described as a disturbance in protein folding, lipid synthesis and calcium ion storage. The ER targeting molecules disrupt its function, thereby increasing the amount of misfolded proteins in the cells. Cancer cells are prone to ER stress due to hypoxia and low pH; in addition, increased cell proliferation leads to a higher rate of protein folding. The higher level of ER stress in cancer cells makes ER a good target for chemotherapeutic agents based on metal complexes. Transition metal complexes of heavy metals can produce ROS after photoirradiation and disrupt the Ca^{2+} levels and their transport in cancer cells. Most of the cationic Ir(III) complexes tested for the anticancer property have N-based ligands such as polypyridyl, N-heterocyclic carbene (NHC), phenanthroline, *etc.*[18] Such cyclometalated Ir(III) complexes can accumulate in the cell membrane and ER membrane and a few can also co-localize in the mitochondria.

The main cause of cell apoptosis in cancer cells is local ROS production and ER stress. Thus, targeting ER for anticancer therapy is an ideal choice but very few neutral Ir(III) complexes having the phenylpyridine/tetrazolato ligand are able to localize in the ER.[31] The glucose- and galactose-linked dipyrrinato complexes **Ir6** and **Ir7** are the neutral molecules reported in this work, which can target ER in the cancer cell line. Sub-cellular studies were carried out using the ER tracker in the cancer cells along with the **Ir6** and **Ir7** complexes. Fig. 8 shows the predominant localization of **Ir6** and **Ir7** in the endoplasmic reticulum, which was further confirmed from their Pearson coefficient (~0.7). The confocal images displayed red luminescent emission from live cells due to **Ir6** and **Ir7**, indicating that glucose- and galactose-linked Ir-dipyrrinato complexes have the potential to be developed as cell-permeable NIR dyes for deep penetration in biological tissues. Furthermore, they can be explored as photochemotherapeutic agents for targeting ER in different kinds of tumors.

Conclusions

A series of luminescent neutral Ir(III) dipyrrinato complexes were synthesized having various chromophores as substituents at the C-5 position of the dipyrrinato ligand. The aromatic substituents in the dipyrrin ligand yielded strong photoluminescence in the red to NIR region (~680–900 nm) along with large Stokes shifts (5910–7045 cm^{-1}). TD-DFT studies indicated significant charge distribution between the dipyrrin ligand and the Ir(III)-cyclometalated unit in all the compounds. X-ray crystal structures revealed an octahedral geometry around the Ir(III) center. The Ir(III) complexes having glucose and galactose sugars on the dipyrrin ligand exhibited strong photoluminescence with maximum Stokes shifts and they showed significant photocytotoxicity in the skin cancer cells. The estimated IC_{50} values in cancer cell lines were between

~17–25 μM for the glycosylated Ir(III) dipyrrinato complexes, making them potential PDT agents. The confocal imaging studies revealed cytoplasmic distribution of glucose/galactose-linked **Ir6** and **Ir7** complexes. Furthermore, sub-cellular studies with different organelle trackers by confocal imaging confirmed their preferential localization in the endoplasmic reticulum. These cell-permeable neutral Ir(III) dipyrrinato complexes with room temperature phosphorescence and significant Stokes shifts can be promising NIR emitters for cellular imaging and as photocytotoxic agents for PDT.

Experimental section

Instruments and reagents

The solvents and reagents were purchased from Aldrich/Acros Organics. A Bruker Avance III 500 MHz NMR spectrometer was used for NMR analysis. The mass spectra were recorded using a Bruker Daltonics UltrafleXtreme MALDI-TOF instrument and a Water Synapt-G2S ESI-Q-TOF instrument was used for ESI-Mass spectra. A Shimadzu UV-1700 spectrophotometer and a JASCO V-750 spectrophotometer were used for absorption studies. A Horiba–Jobin Yvon Fluolorog-3 spectrofluorometer was used for fluorescence experiments. An OBIS Laser 488 (15 mW) and an Oxxius Laser 532 (15 mW) were used for the singlet oxygen experiment.

Computational methodology

All the density functional theory (DFT) calculations were performed with the Gaussian-09 program package.[54] The ground-state (S_0) geometry optimization was carried out without symmetry constraints using the Becke three-parameter Lee–Yang–Parr functional B3LYP[55–57] along with a valence double-ζ 6-31G (d) basis set for all the atoms except iridium and iodine for which LANL2DZ[58] was used. The Hessian matrix was calculated analytically at the same level of approximation to affirm that the given structure is at its minima on the potential energy surface. Subsequently, the vertical electronic excitation energies were determined for the S_0 optimized geometries using B3LYP[55–57] along with the 6-31G(d) and LANL2DZ[58] basis sets for the lighter and heavier atoms, respectively. The choice of the functional was made from its efficiency on a wide range of compounds documented in the literature. The effect of DMSO was modeled by using a conductor-like polarizable continuum model (C-PCM)[59,60] at default parameters.

Biological studies

The cytotoxicity studies of **Ir6**, **Ir7**, **WS-Ir6** and **WS-Ir7** along with the free ligand were done using the MTT (3-(4,5-dimethylthiazol-2-yl)-2,5-diphenyltetrazolium bromide) assay. A549 and HaCaT cells were used and 10 000 cells were plated around separately. In two different 96-well culture plates, the cells were incubated for 24 hours with varying concentrations following serial dilution from 100 μM to 0.78 μM in 1% DMSO/DMEM. A PBS solution was used to wash the cells in both the plates. The cells are divided into two sets; one was kept in the dark and the other was used for light activity. Light treatment (λ = 400–700 nm, light dose = 10 J cm^{-2} for 1 h) was given with a Luzchem Photoreactor (Model LZC-1, Ontario, Canada) consisting of 8 white fluorescent tubes (Sylvania make). Readings were taken through a TECAN microplate reader and the data were plotted using the software GraphPad Prism 6.

Confocal imaging

Compounds **Ir6** and **Ir7** were investigated for their cellular localization using confocal microscopy and the images were collected with a magnification of 63× in a Leica microscope (TCS, SP5). The concentration used for **Ir6** and **Ir7** was 10 μM in 1% DMSO/DMEM. The images were obtained after 24 h incubation in HaCaT cells. 12-well plates were used to grow the cells for 24 h, where each well contains 3 × 10^4 cells in media. DAPI (1 mg mL^{-1}) was used for nuclear staining for 5 min. For further subcellular localization, live cells were stained with the endoplasmic reticulum green trackers (ERGT).

Synthesis of starting materials

The required aldehydes[61–64] or dipyrromethanes,[11,40,41] cyclometalated iridium,[39,42] and 2,3,4,6-tetra-*O*-acetyl-glucosyl/galactosyl-1-thioacetate for metal dipyrrinate synthesis were prepared by the literature-reported methods.

General synthesis of iridium dipyrrinates (Ir1–Ir5)

Iridium dipyrrinates were synthesized by following the reported method with certain modifications.[41] Under an inert atmosphere, a solution of dipyrromethane (1 equiv., 0.14 mmol) and DDQ (1 equiv., 32 mg, 0.14 mmol) in dry THF (7 mL) was allowed to stir for 1 h at room temperature. Later on, potassium carbonate (14 equiv., 286 mg, 2.07 mmol) was added and further stirred for 15 min followed by the addition of cyclometalated iridium (0.5 equiv., 80 mg, 0.07 mmol) and allowed to reflux for 12 h. Reaction progress was monitored by TLC, and the initial dipyrrin spot vanished and a new orange spot was observed in TLC. The reaction mixture was subjected to vacuum filtration, and the obtained solid residue (metal salt) was washed with DCM (3 × 25 mL). The collected filtrate was then evaporated to dryness under reduced pressure. The desired compound was purified using a neutral alumina column with a 25–40% DCM/hexane mixture.

Ir1: The general procedure was followed using 2,2′-(thiophen-2-ylmethylene)bis(1*H*-pyrrole) (1 equiv., 32 mg, 0.14 mmol). Column condition: 25–30% DCM/hexane. Orange solid. Yield: (74 mg, 73%); m.p. >350 °C; IR (neat, cm^{-1}): 3109, 3031, 2925, 2855, 1603, 1580, 1559, 1523, 1473, 1435, 1416, 1405, 1374, 1335, 1313, 1265, 1239, 1215, 1096, 1060, 1025, 982, 888, 862, 833, 809, 798, 762, 756, 731, 721, 666, 629, 616, 588, 557, 502; ^{1}H NMR (500 MHz, CD_2Cl_2) δ ppm: 7.88–7.84 (m, 4H, Ar–*H*), 7.69–7.65 (m, 4H, Ar–*H*), 7.49 (d, J = 5 Hz, 1H, Ar–*H*), 7.29 (d, J = 2.5 Hz, 1H, Ar–*H*), 7.12 (t, J = 3.5 Hz, 1H, Ar–*H*), 6.98–6.94 (m, 4H, Ar–*H*), 6.85–6.81 (m, 4H, Ar–H, α-pyrrolic–*H*), 6.78 (s, 2H, β-pyrrolic–*H*), 6.37 (d, J = 7.5 Hz, 2H, Ar–*H*), 6.25 (d, J = 4 Hz, 2H, β-pyrrolic–*H*); ^{13}C NMR (125.76 MHz, CD_2Cl_2) δ ppm: 168.5, 156.3, 152.6, 149.5, 144.7,

140.5, 139.9, 136.2, 134.7, 132.0, 131.2, 130.3, 129.4, 126.3, 125.9, 123.9, 122.1, 120.8, 118.7, 117.1; MALDI-MS: $C_{35}H_{25}IrN_4S^+$ $[M]^+$: calcd *m*/*z*† 726.142, found *m*/*z* 726.254.

Ir2: The general procedure was followed using 9-butyl-3-(di(1*H*-pyrrol-2-yl)methyl)-9*H*-carbazole (1 equiv., 52 mg, 0.14 mmol). Column condition: 32–35% DCM/hexane. Orange solid. Yield: (97 mg, 78%); m.p. >350 °C; IR (neat, cm^{-1}): 3045, 2922, 2852, 1712, 1626, 1603, 1581, 1560, 1534, 1474, 1437, 1406, 1374, 1341, 1265, 1242, 1212, 1188, 1155, 1061, 1123, 1024, 984, 895, 882, 835, 799, 752, 722, 667, 648, 630, 623, 610, 600, 558, 544; ^{1}H NMR (500 MHz, CD_2Cl_2) δ ppm: 8.19 (d, J = 1.5 Hz, 1H, Ar–*H*), 8.06 (d, J = 8 Hz, 1H, Ar–*H*), 7.94–7.89 (m, 4H, Ar–*H*), 7.58 (dd, J = 7 Hz, 1.5 Hz, 1H, Ar–*H*), 7.50–7.46 (m, 3H, Ar–*H*), 7.24–7.22 (m, 1H, Ar–*H*), 7.05–6.96 (m, 4H, Ar–*H*), 6.85 (t, J = 7.5 Hz, 2H, Ar–*H*), 6.81 (d, J = 1.5 Hz, 2H, α-pyrrolic–*H*), 6.57 (dd, J = 3 Hz, 1 Hz, 2H, β-pyrrolic–*H*), 6.42 (q, J = 3.5 Hz, 2H, Ar–*H*), 6.23 (dd, J = 3 Hz, 1 Hz, 2H, β-pyrrolic–*H*), 4.39 (t, J = 7 Hz, 2H, N–CH_2–C–), 1.95–1.89 (m, 2H, –C–CH_2–C–), 1.49–1.45 (m, 2H, –C–CH_2–CH$_3$), 0.99 (t, J = 7.5 Hz, 3H, –C–CH_3); ^{13}C NMR (125.76 MHz, CD_2Cl_2) δ ppm: 168.7, 156.7, 151.7, 151.6, 149.9, 149.6, 144.7, 141.0, 140.3, 136.2, 135.2, 132.1, 130.3, 129.4, 128.6, 125.7, 123.9, 122.7, 122.6, 122.1, 121.5, 120.8, 120.3, 118.9, 118.7, 116.8, 108.9, 107.0, 43.0, 31.1, 20.5, 13.6; MALDI-MS: $C_{47}H_{38}IrN_5^+$ $[M]^+$: calcd *m*/*z* 865.275, found *m*/*z* 865.510.

Ir3: The general procedure was followed using 9-butyl-3-(5-(di(1*H*-pyrrol-2-yl)methyl)thiophen-2-yl)-9*H*-carbazole (1 equiv., 63 mg, 0.14 mmol). Column condition: 33–40% DCM/hexane. Orange solid. Yield: (94 mg, 71%); m.p. 315–317 °C; IR (neat, cm^{-1}): 3046, 2955, 2923, 2853, 1711, 1604, 1581, 1560, 1530, 1474, 1449, 1437, 1406, 1374, 1340, 1304, 1264, 1242, 1214, 1192, 1155, 1123, 1061, 1025, 983, 888, 838, 824, 797, 753, 728, 720, 702, 667, 629, 599, 586, 558; ^{1}H NMR (500 MHz, CD_2Cl_2) δ ppm: 8.39 (d, J = 1.5 Hz, 1H, Ar–*H*), 8.15 (d, J = 8 Hz, 1H, Ar–*H*), 7.90–7.86 (m, 4H, Ar–*H*), 7.80 (dd, J = 6.5 Hz, 2 Hz, 1H, Ar–*H*), 7.71–7.66 (m, 4H, Ar–*H*), 7.50–7.47 (m, 3H, Ar–*H*), 7.40 (d, J = 3.5 Hz, 1H, Ar–*H*), 7.31 (d, J = 3.5 Hz, 2H, Ar–*H*), 7.28–7.23 (dt, J = 3 Hz, 1 Hz, 1H, Ar–*H*), 7.07 (dd, J = 1.5 Hz, 2.5 Hz, 2H, α-pyrrolic–*H*), 7.00–6.95 (m, 4H, Ar–*H*), 6.85 (dt, J = 6 Hz, 1 Hz, 2H, Ar–*H*), 6.81 (d, J = 1.5 Hz, 2H, β-pyrrolic–*H*), 6.40 (dd, J = 7 Hz, 0.5 Hz, 2H, Ar–*H*), 6.29 (dd, J = 3 Hz, 1 Hz, 2H, β-pyrrolic–*H*), 4.34 (t, J = 7 Hz, 2H, N–CH_2–C–), 1.90–1.86 (m, 2H, –C–CH_2–C–), 1.45–1.38 (m, 2H, –C–CH_2–CH$_3$), 0.97 (t, J = 7.5 Hz, 3H, –C–CH_3); ^{13}C NMR (125.76 MHz, CD_2Cl_2) δ ppm: 168.6, 156.4, 152.5, 149.6, 147.1, 144.7, 141.0, 140.7, 140.2, 138.0, 136.2, 134.6, 132.1, 131.6, 131.3, 129.4, 126.0, 125.0, 123.9, 123.2, 122.6, 122.1, 121.0, 120.8, 120.3, 119.0, 118.7, 117.5, 117.1, 109.2, 109.0, 43.0, 31.0, 20.5, 13.6; MALDI-MS: $C_{51}H_{40}IrN_5S^+$ $[M]^+$: calcd *m*/*z* 947.263, found *m*/*z* 947.983.

Ir4: The general procedure was followed using 5-(5-(di(1*H*-pyrrol-2-yl)methyl)thiophen-2-yl)benzo[*c*][1,2,5]thiadiazole (1 equiv., 51 mg, 0.14 mmol). Column condition: 35–40% DCM/hexane. Orange solid. Yield: (83 mg, 69%); m.p. 306–308 °C; IR (neat, cm^{-1}): 3050, 2923, 2849, 1604, 1581, 1538, 1474, 1406, 1376, 1342, 1266, 1245, 1193, 1161, 1062, 1025, 984, 890, 828, 789, 758, 721, 667. 630; ^{1}H NMR (500 MHz, CD_2Cl_2) δ ppm: 8.13 (d, J = 3.5 Hz, 1H Ar–*H*), 7.96–7.93 (m, 2H, Ar–*H*), 7.89–7.87 (m, 4H, Ar–*H*), 7.70–7.65 (m, 5H, Ar–*H*), 7.39–7.38 (m, 1H, Ar–*H*), 7.00–6.95 (m, 6H, Ar–*H*, β-pyrrolic–*H*), 6.84 (t, J = 7.5 Hz, 2H, Ar–*H*), 6.81 (d, J = 1 Hz, 2H, α-pyrrolic–*H*), 6.38 (d, J = 7.5 Hz, 2H, Ar–*H*), 6.28 (d, J = 4 Hz, 2H, β-pyrrolic–*H*); ^{13}C NMR (125.76 MHz, CD_2Cl_2) δ ppm: 168.6, 156.2, 155.6, 152.8, 152.1, 149.6, 144.7, 141.5, 140.3, 140.0, 136.3, 134.4, 132.1, 131.2, 131.1, 129.6, 129.5, 127.1, 126.6, 125.2, 123.9, 122.1, 120.8, 120.2, 118.7, 117.3; MALDI-MS: $C_{41}H_{27}IrN_6S_2^+$ $[M]^+$: calcd *m*/*z* 860.136, found *m*/*z* 860.125.

Ir5: The general procedure was followed using 2,2′-((perfluorophenyl)methylene)bis(1*H*-pyrrole) (1 equiv., 44 mg, 0.14 mmol). Column condition: 30–35% DCM/hexane. Orange solid. Yield: (92 mg, 81%); m.p. 186–188 °C; IR (neat, cm^{-1}): 3109, 3050, 3053, 2924, 1652, 1606, 1581, 1548, 1526, 1514, 1495, 1473, 1438, 1416, 1375, 1340, 1312, 1266, 1245, 1216, 1191, 1158, 1146, 1125, 1078, 1060, 1018, 994, 977, 948, 887, 837, 795, 749, 731, 724, 705, 668, 643, 630, 598, 557; ^{1}H NMR (500 MHz, CD_2Cl_2) δ ppm: 7.92 (dd, J = 0.5 Hz, 4.5 Hz, 2H, Ar–*H*), 7.88 (d, J = 8 Hz, 2H, Ar–*H*), 7.71–7.65 (m, 4H, Ar–*H*), 6.99–6.94 (m, 4H, Ar–*H*), 6.84 (dt, J = 6 Hz, 1.5 Hz, 2H, Ar–*H*), 6.79 (s, 2H, α-pyrrolic–*H*), 6.47 (d, J = 4 Hz, 2H, β-pyrrolic–*H*), 6.38 (d, J = 7.5 Hz, 2H, Ar–*H*), 6.28 (dd, J = 3.5 Hz, 1 Hz, 2H, β-pyrrolic–*H*); ^{13}C NMR (125.76 MHz, CD_2Cl_2) δ ppm: 168.5, 155.5, 153.8, 149.6, 144.7, 136.5, 133.2, 132.1, 129.5, 129.4, 123.9, 122.1, 121.0, 118.8, 118.3; ^{19}F NMR (470.4 MHz, CD_2Cl_2) δ ppm: −140.94 (m, 2F), −154.95 (t, J = 23.5 Hz, 18.8 Hz, 1F), −162.63 (m, 2F); MALDI-MS: $C_{37}H_{22}F_5IrN_4^+$ $[M]^+$: calcd *m*/*z* 810.139, found *m*/*z* 810.170.

General synthesis of glycosylated iridium complexes (Ir6 and Ir7)

In a 25 mL round bottom flask, **Ir5** (1 equiv., 85 mg, 0.10 mmol) was mixed with 2,3,4,6-tetra-*O*-acetyl-glucosyl/galactosyl-1-thioacetate (2 equiv., 82 mg, 0.20 mmol) in 10 mL of dry DMF for 5 min. Then the reaction mixture was treated with base DEA (0.41 mL) and stirred for 12 h at room temperature. The progress of the reaction was monitored with TLC which showed a new spot being formed. After workup with ethyl acetate and water, the organic layer was dried over anhydrous Na_2SO_4. The crude reaction mixture was purified by using alumina column chromatography and the desired product was obtained in 30% ethyl acetate/hexane. The water-soluble derivatives **WS-Ir6** and **WS-Ir7** were prepared by the deprotection of acetylated glucose/galactose units by treating **Ir6** and **Ir7** with a base in methanol for 3 hours.[51] The water-soluble derivatives **WS-Ir6** and **WS-Ir7** were collected in 45% to 54% yields after amberlyst treatment and filtration to remove the salt.

Ir6: Column condition: 30–35% ethylacetate/hexane. Orange solid. Yield: (95 mg, 78%); m.p. 258–260 °C; IR (neat, cm^{-1}): 3042, 2925, 2853, 1747, 1605, 1582, 1550, 1474, 1417, 1375, 1342, 1247, 1216, 1161, 1084, 1059, 1020, 983, 969, 917, 888, 836, 757, 742, 731, 668, 630, 599, 560; ^{1}H NMR (500 MHz, CD_2Cl_2) δ ppm: 7.93 (dd, J = 0.5 Hz, 5.5 Hz, 2H, Ar–*H*), 7.88 (d, J = 8.5 Hz, 2H, Ar–*H*), 7.71–7.65 (m, 4H, Ar–*H*), 6.99–6.94 (m,

4H, Ar–*H*), 6.84 (dt, *J* = 6.5 Hz, 1 Hz, 2H, Ar–*H*), 6.80 (s, 2H, α-pyrrolic–*H*), 6.51 (d, *J* = 4.5 Hz, 2H, β-pyrrolic–*H*), 6.39 (d, *J* = 7.5 Hz, 2H, Ar–*H*), 6.28 (dd, *J* = 3 Hz, 1 Hz, 2H, β-pyrrolic–*H*), 5.43 (d, *J* = 3.5 Hz, 1H), 5.26 (dt, *J* = 6 Hz, 4 Hz, 1H), 5.08 (m, 1H), 4.90 (d, *J* = 10 Hz, 1H), 4.15–4.07 (m, 2H), 3.95 (t, *J* = 6.5 Hz, 1H), 2.16 (d, *J* = 8.5 Hz, 6H), 1.98 (s, 6H); ^{13}C NMR (125.76 MHz, CD_2Cl_2) *δ* ppm: 170.1, 170.0, 169.8, 169.4, 168.4, 155.4, 153.8, 149.6, 144.7, 136.4, 132.9, 132.1, 129.5, 129.4, 123.9, 122.1, 121.0, 118.8, 118.3, 85.8, 75.0, 71.7, 67.7, 67.1, 61.4, 20.3; ^{19}F NMR (470.4 MHz, CD_2Cl_2) *δ* ppm: −132.52 (m, 2F), −140.37 (m, 2F); MALDI-MS: $C_{51}H_{42}F_4IrN_4O_9S^+$ $[M + H]^+$: calcd *m*/*z* 1155.223, found *m*/*z* 1155.752.

Ir7: Column condition: 30–35% ethylacetate/hexane. Orange solid. Yield: (101 mg, 83%); m.p. 184–186 °C; IR (neat, cm^{-1}): 3058, 2924, 2853, 1748, 1605, 1581, 1552, 1474, 1438, 1417, 1376, 1342, 1246, 1216, 1161, 1092, 1060, 1021, 984, 969, 912, 888, 837, 793, 782, 756, 742, 733, 705, 668, 630, 599, 558; ^{1}H NMR (500 MHz, CD_2Cl_2) *δ* ppm: 7.93 (d, *J* = 5.5 Hz, 2H, Ar–*H*), 7.88 (d, *J* = 8 Hz, 2H, Ar–*H*), 7.70–7.65 (m, 4H, Ar–*H*), 6.99–6.94 (m, 4H, Ar–*H*), 6.84 (t, *J* = 7.5 Hz, 2H, Ar–*H*), 6.80 (d, *J* = 1 Hz, 2H, α-pyrrolic–*H*), 6.52 (s, 2H, β-pyrrolic–*H*), 6.39 (d, *J* = 7.5 Hz, 2H, Ar–*H*), 6.28 (d, *J* = 4 Hz, 2H, β-pyrrolic–*H*), 5.25 (dt, *J* = 1 Hz, 8.5 Hz, 1H), 5.11–5.01 (m, 2H), 4.92 (dd, *J* = 1 Hz, 9 Hz, 1H), 4.22–4.19 (m, 1H), 4.13–4.10 (m, 1H), 3.76–3.73 (m, 1H), 2.10 (s, 3H), 1.99 (s, 9H); ^{13}C NMR (125.76 MHz, CD_2Cl_2) *δ* ppm: 170.2, 169.8, 169.3, 169.2, 168.4, 155.4, 153.8, 149.6, 144.7, 136.4, 132.8, 132.1, 131.0, 129.5, 129.4, 123.9, 122.1, 121.0, 118.8, 118.3, 113.7, 84.9, 76.3, 73.6, 70.5, 68.0, 61.8, 29.6, 20.3; ^{19}F NMR (470.4 MHz, CD_2Cl_2) *δ* ppm: −132.25 (m, 2F), −140.21 (m, 2F); MALDI-MS: $C_{51}H_{42}F_4IrN_4O_9S^+$ $[M + H]^+$: calcd *m*/*z* 1155.223, found *m*/*z* 1155.226.

WS-Ir6: Orange solid. Yield: (54%); IR (neat, cm^{-1}): 3352, 2934, 2853, 1605, 1660, 1556, 1467, 1377, 1344, 1247, 1024.18, 986; MALDI-MS: $C_{43}H_{33}F_4IrN_4O_5S^+$ $[M + H]^+$: calcd *m*/*z* 986.031, found *m*/*z* 986.251.

WS-Ir7: Orange solid. Yield: (45%); IR (neat, cm^{-1}): 3362, 2953, 2853, 1659, 1631, 1467, 1247, 1027; MALDI-MS: $C_{43}H_{33}F_4IrN_4O_5S^+$ $[M + H]^+$: calcd *m*/*z* 986.031, found *m*/*z* 986.410.

Synthesis of the modified complex Ir8

5,5′-((Perfluorophenyl)methylene)bis(2,4-dimethyl-1*H*-pyrrole). Compound **A**: The synthetic methodology from the reported procedure was followed after certain modifications.[65] Pentafluorobenzaldehyde (1 equiv., 2 g, 10.51 mmol) and 2,4-dimethylpyrrole (2 equiv., 2 g, 21.02 mmol) were dissolved in 100 mL of DCM under an inert atmosphere. After 5 min of stirring, TFA (0.1 equiv., 80 μL, 1.05 mmol) was added which results in a color change to red. The reaction was allowed to stir for 2 h at rt and the progress of the reaction was checked with TLC. The solvent was removed under reduced pressure before loading the reaction mixture to a silica column and the desired compound was collected in 25% DCM/hexane. Brown solid obtained. Yield: (1.55 g, 40%); ^{1}H NMR ($CDCl_3$, 500 MHz, *δ* ppm): 7.66 (s, 2H, N–*H*), 5.87 (s, 1H, *meso*-*H*), 5.67 (s, 2H, β-pyrrolic–*H*), 2.19 (s, 6H, –C*H*$_3$), 1.85 (s, 6H, –C*H*$_3$); ^{13}C NMR (125.7 MHz, $CDCl_3$, *δ* ppm): 154.1, 140.12, 135.9, 119.2, 85.0, 53.4, 17.2, 16.0; HRMS (ESI-Q-TOF): $C_{19}H_{16}F_5N_2^+$ $[M - H]^+$ calcd: *m*/*z* 367.123; found: *m*/*z* 367.1806.

(*Z*)-3-Iodo-5-((4-iodo-3,5-dimethyl-2*H*-pyrrol-2-ylidene)(perfluorophenyl)methyl)-2,4-dimethyl-1*H*-pyrrole. Compound **B**: Synthetic methodology followed from a reported procedure after slight modifications.[66,67] 5,5′-((Perfluorophenyl)methylene)bis(2,4-dimethyl-1*H*-pyrrole) (1 equiv., 500 mg, 1.35 mmol) in methanol (10 mL) was stirred for 5 min. The temperature was maintained up to 0 °C and then resublimed iodine (2.2 equiv., 758 mg, 2.98 mmol) was added followed by the addition of the base potassium carbonate (3 equiv., 560 mg, 4.05 mmol) and stirring for 12 h at 0 °C. The colour of the reaction mixture turned orange. The progress of the reaction was checked by TLC before quenching the reaction. The solvent was removed under reduced pressure, workup was performed with DCM and saturated sodium thiosulfate (25 mL × 3) and then dried over $MgSO_4$. The reaction mixture was then subjected for purification by silica gel column chromatography and the pure compound was collected in 10% DCM/hexane. Red solid obtained. Yield: (634 mg, 76%); ^{1}H NMR ($CDCl_3$, 500 MHz) *δ* ppm: 13.59 (s, 1H, N–*H*), 2.41 (s, 6H, –C*H*$_3$), 1.53 (s, 6H, –C*H*$_3$); ^{13}C NMR (125.7 MHz, $CDCl_3$) *δ* ppm: 154.1, 145.4, 140.1, 136.0, 119.2, 112.0, 85.0, 17.2, 16.0; ^{19}F NMR (470.4 MHz, $CDCl_3$) *δ* ppm: −139.79 (t, *J* = 14.1 Hz, 9.4 Hz, 2F), −151.48 (m, 2F), −160.21 (m, 2F); ESI-MS: $C_{19}H_{14}F_5I_2N_2^+$ $[M + H]^+$ calcd: *m*/*z* 618.916; found: *m*/*z* 618.9987.

Ir8: The general synthesis method was followed as for iridium dipyrrinates using (*Z*)-3-iodo-5-((4-iodo-3,5-dimethyl-2*H*-pyrrol-2-ylidene)(perfluorophenyl)methyl)-2,4-dimethyl-1*H*-pyrrole (1 equiv., 45 mg, 0.07 mmol) and K_2CO_3 (14 equiv., 141 mg, 1.01 mmol) was dissolved in dry THF (4 mL) and stirred for 15 min followed by the addition of cyclometalated iridium (1 equiv., 80 mg, 0.07 mmol) and allowed to reflux for 12 h. The reaction progress was monitored by TLC and the initial dipyrrin spot vanished and a new orange spot was observed in TLC. The reaction mixture was cooled down to room temperature and subjected to vacuum filtration. The solids were removed and washed with DCM (3 × 25 mL). The collected filtrate was then evaporated to dryness under reduced pressure. The desired compound was purified using a neutral alumina column with a 10–14% DCM/hexane mixture.

Orange solid. Yield: (59 mg, 76%); m.p. 255–257 °C; IR (neat, cm^{-1}): 3038, 2925, 1654, 1604, 1582, 1522, 1495, 1473, 1436, 1409, 1374, 1356, 1318, 1264, 1225, 1158, 1118, 1059, 1029, 824, 773, 754, 731, 712, 700, 674, 666, 634, 589, 550; ^{1}H NMR (500 MHz, CD_2Cl_2) *δ* ppm: 8.45 (d, *J* = 5.5 Hz, 2H, Ar–*H*), 7.84 (d, *J* = 8 Hz, 2H, Ar–*H*), 7.78–7.75 (m, 2H, Ar–*H*), 7.55 (d, *J* = 8 Hz, 2H, Ar–*H*), 7.11–7.08 (m, 2H, Ar–*H*), 6.85–6.82 (m, 2H, Ar–*H*), 6.66–6.62 (m, 2H, Ar–*H*), 6.25 (d, *J* = 7.5 Hz, 2H, Ar–*H*), 1.46 (s, 6H, –C*H*$_3$), 1.41 (s, 6H, –C*H*$_3$); ^{13}C NMR (125.76 MHz, CD_2Cl_2) *δ* ppm: 168.2, 163.4, 152.7, 151.8, 144.5, 142.3, 136.6, 134.0, 132.3, 128.1, 123.7, 121.8, 123.7, 121.8, 120.8, 118.4, 88.1, 19.3, 18.3; ^{19}F NMR (470.4 MHz, CD_2Cl_2) *δ* ppm: −139.94 (m, 2F), −153.45 (t, *J* = 23.5 Hz, 18.8 Hz, 1F), −161.64 (m, 2F); MALDI-MS: $C_{41}H_{28}F_5I_2IrN_4^+$ $[M]^+$: calcd *m*/*z* 1117.995, found *m*/*z* 1117.154.

Conflicts of interest

The authors declare no competing financial interest.

Acknowledgements

Financial and infrastructural support from IIT Gandhinagar is gratefully acknowledged. NM and MYL thank IIT Gandhinagar for the fellowship. JC thanks the DST, Govt. of India for the INSPIRE fellowship (IF190158). Author also thanks Prof. A. R. Chakravarty (IISc) for providing the cell culture facility. IG thanks Dr Saumyakanti Khatua, IIT Gandhinagar for providing the laser facility.

References

1 G. Gupta, A. Das, J. Lee, N. Mandal and C. Y. Lee, *Inorg. Chem. Commun.*, 2020, **113**, 107759.
2 K. Muthukumaran, S. H. H. Zaidi, L. Yu, P. Thamyongkit, M. E. Calder, D. S. Sharada and J. S. Lindsey, *J. Porphyrins Phthalocyanines*, 2005, **9**, 745–759.
3 S. A. Baudron, *Dalton Trans.*, 2013, **42**, 7498–7509.
4 S. A. Baudron, *CrystEngComm*, 2010, **12**, 2288–2295.
5 T. E. Wood and A. Thompson, *Chem. Rev.*, 2007, **107**, 1831–1861.
6 R. Shikha Singh, R. P. Prasad, R. K. Gupta and D. P. Shankar, *Coord. Chem. Rev.*, 2020, **414**, 213269.
7 V. Mani, V. G. Krishnakumar, S. Gupta, S. Mori and I. Gupta, *Sens. Actuators, B*, 2017, **244**, 673–683.
8 P. E. Kesavan, V. Pandey, M. K. Raza, S. Mori and I. Gupta, *Bioorg. Chem.*, 2019, **91**, 103139.
9 G. Ulrich, R. Ziessel and A. Harriman, *Angew. Chem., Int. Ed.*, 2008, **47**, 1184–1201.
10 I. Gupta and P. E. Kesavan, *Front. Chem.*, 2019, **7**, 841.
11 P. E. Kesavan and I. Gupta, *Dalton Trans.*, 2014, **43**, 12405–12413.
12 N. Balsukuri, M. Y. Lone, P. C. Jha, S. Mori and I. Gupta, *Chem. – Asian J.*, 2016, **11**, 1572–1587.
13 N. Balsukuri, S. Mori and I. Gupta, *J. Porphyrins Phthalocyanines*, 2016, **20**, 719–729.
14 N. Balsukuri, N. Manav, M. Y. Lone, S. Mori, A. Das, P. Sen and I. Gupta, *Dyes Pigm.*, 2020, **176**, 108249.
15 M. Vedamalai, D. Kedaria, R. Vasita, S. Mori and I. Gupta, *Dalton Trans.*, 2016, **45**, 2700–2708.
16 C. Imberti, P. Zhang, H. Huang and P. Sadler, *J. Angew. Chem., Int. Ed.*, 2020, **59**, 61–73.
17 S. Monro, K. L. Colón, H. Yin, J. Roque, P. Konda, S. Gujar, R. P. Thummel, L. Lilge, C. G. Cameron and S. A. McFarland, *Chem. Rev.*, 2019, **119**, 797–828.
18 A. P. King and J. Wilson, *Chem. Soc. Rev.*, 2020, **49**, 8113–8136.
19 A. Zamora, G. Vigueras, V. Rodríguez, M. D. Santana and J. Ruiz, *Coord. Chem. Rev.*, 2018, **360**, 34–76.
20 M. Dickerson, Y. Sun, B. Howerton and E. C. Glazer, *Inorg. Chem.*, 2014, **53**, 10370–10377.
21 Y.-L. Wang, Y.-H. Lee, I.-J. Chiu, Y.-F. Lin and H.-W. Chiu, Potent Impact of Plastic Nanomaterials and Micromaterials on the Food Chain and Human Health, *Int. J. Mol. Sci.*, 2020, **21**(5), 1727.
22 B. Yuan, J. Liu, R. Guan, C. Jin, L. Ji and H. Chao, *Dalton Trans.*, 2019, **48**, 6408–6415.
23 S. Banerjee, A. Dixit, R. N. Shridharan, A. A. Karande and A. R. Chakravarty, *Chem. Commun.*, 2014, **50**, 5590–5592.
24 Y. K. Maurya, T. Ishikawa, Y. Kawabe, M. Ishida, M. Toganoh, S. Mori, Y. Yasutake, S. Fukatsu and H. Furuta, *Inorg. Chem.*, 2016, **55**, 6223–6230.
25 M. L. P. Reddy and K. S. Bejoymohandas, *J. Photochem. Photobiol., C*, 2016, **29**, 29–47.
26 K. K. W. Lo, *Acc. Chem. Res.*, 2015, **48**, 2985–2995.
27 D. L. Ma, D. S. H. Chan and C. H. Leung, *Acc. Chem. Res.*, 2014, **47**, 3614–3631.
28 X. Y. Ren, Y. Wu, G. G. Shan, L. Wang, Y. Geng and Z. M. Su, *RSC Adv.*, 2014, **4**, 62197–62208.
29 R. Cao, J. Jia, X. Ma, M. Zhou and H. Fei, *J. Med. Chem.*, 2013, **56**, 3636–3644.
30 S. Mandal, D. K. Poria, R. Ghosh, P. S. Ray and P. Gupta, *Dalton Trans.*, 2014, **43**, 17463–17474.
31 J. S. Nam, M. G. Kang, J. Kang, S. Y. Park, S. J. C. Lee, H. T. Kim, J. K. Seo, O. H. Kwon, M. H. Lim, H. W. Rhee and T. H. Kwon, *J. Am. Chem. Soc.*, 2016, **138**, 10968–10977.
32 C. Caporale, C. A. Bader, A. Sorvina, K. D. M. MaGee, B. W. Skelton, T. A. Gillam, P. J. Wright, P. Raiteri, S. Stagni, J. L. Morrison, S. E. Plush, D. A. Brooks and M. Massi, *Chem. – Eur. J.*, 2017, **23**, 15666–15679.
33 K. Y. Zhang, S. P. Y. Li, N. Zhu, L. W. S. Or, M. S. H. Cheung, Y. W. Lam and K. K. W. Lo, *Inorg. Chem.*, 2010, **49**, 2530–2540.
34 C. Ulbricht, B. Beyer, C. Friebe, A. Winter and U. S. Schubert, *Adv. Mater.*, 2009, **21**, 4418–4441.
35 K. K. W. Lo, K. Y. Zhang, C. K. Chung and K. Y. Kwok, *Chem. – Eur. J.*, 2007, **13**, 7110–7120.
36 S. Zhang, M. Hosaka, T. Yoshihara, K. Negishi, Y. Iida, S. Tobita and T. Takeuchi, *Cancer Res.*, 2010, **70**, 4490–4498.
37 B. F. Hohlfeld, B. Gitter, C. J. Kingsbury, K. J. Flanagan, D. Steen, G. D. Wieland, N. Kulak, M. O. Senge and A. Wiehe, *Chem. – Eur. J.*, 2021, **27**, 6440–6459.
38 M. Nonoyama, *Bull. Chem. Soc. Jpn.*, 1974, **47**, 767–768.
39 V. Pandey, M. K. Raza, M. Sonowal and I. Gupta, *Bioorg. Chem.*, 2021, **106**, 104467.
40 N. Manav, P. E. Kesavan, M. Ishida, S. Mori, Y. Yasutake, S. Fukatsu, H. Furuta and I. Gupta, *Dalton Trans.*, 2019, **48**, 2467–2478.
41 B. J. Littler, M. A. Miller, C. H. Hung, R. W. Wagner, D. F. O'Shea, P. D. Boyle and J. S. Lindsey, *J. Org. Chem.*, 1999, **64**, 1391–1396.
42 K. Hanson, A. Tamayo, V. V. Diev, M. T. Whited, P. I. Djurovich and M. Thompson, *Inorg. Chem.*, 2010, **49**, 6077–6084.

43 S. Das and I. Gupta, *Inorg. Chem. Commun.*, 2015, **60**, 54–60.
44 K. Takaki, E. Sakuda, A. Ito, S. Horiuchi, Y. Arikawa and K. Umakoshi, *Inorg. Chem.*, 2019, **58**, 14542–14550.
45 P. Pushpanandan, Y. K. Maurya, T. Omagari, R. Hirosawa, M. Ishida, S. Mori, Y. Yasutake, S. Fukatsu, J. Mack, T. Nyokong and H. Furuta, *Inorg. Chem.*, 2017, **56**, 12572–12580.
46 L. V. Lutkus, S. S. Rickenbach and T. M. McCormick, *J. Photochem. Photobiol., A*, 2019, **378**, 131–135.
47 V. Pandey, M. K. Raza, P. Joshi and I. Gupta, *J. Org. Chem.*, 2020, **85**, 6309–6322.
48 S. Moromizato, Y. Hisamatsu, T. Suzuki, Y. Matsuo, R. Abe and S. Aoki, *Inorg. Chem.*, 2012, **51**, 12697–12706.
49 A. Aggarwal, S. Thompson, S. Singh, B. Newton, A. Moore, R. Gao, X. Gu, S. Mukherjee and C. M. Drain, *Photochem. Photobiol.*, 2014, **90**, 419–430.
50 N. Epelde-Elezcano, V. Martínez-Martínez, E. Peña-Cabrera, C. F. A. Gómez-Durán, L. L. Arbeloa and S. Lacombe, *RSC Adv.*, 2016, **6**, 41991–41998.
51 G. Zhang, H. Zhang, Y. Gao, R. Tao, L. Xin and J. Yi, *Organometallics*, 2014, **33**, 61–68.
52 K. Yokoi, C. Balachandran, M. Umezawa, K. Tsuchiya, A. Mitrić and S. Aoki, *ACS Omega*, 2020, **5**, 6983–7001.
53 A. Prokop, J. A. Czaplewska, M. Clausen, M. König, A. Wild, R. Thorwirth, B. Schulze, K. Babiuch, D. Pretzel, U. S. Schubert and M. Gottschaldt, *Eur. J. Inorg. Chem.*, 2016, **21**, 3480–3488.
54 M. J. Frisch, G. W. Trucks, H. B. Schlegel, G. E. Scuseria, M. A. Robb, J. R. Cheeseman, G. Scalmani, V. Barone, B. Mennucci, G. A. Petersson, H. Nakatsuji, M. Caricato, X. Li, H. P. Hratchian, A. F. Izmaylov, J. Bloino, G. Zheng, J. L. Sonnenberg, M. Hada, M. Ehara, K. Toyota, R. Fukuda, J. Hasegawa, M. Ishida, T. Nakajima, Y. Honda, O. Kitao, H. Nakai, T. Vreven, J. A. Montgomery, Jr., J. E. Peralta, F. Ogliaro, M. Bearpark, J. J. Heyd, E. Brothers, K. N. Kudin, V. N. Staroverov, R. Kobayashi, J. Normand, K. Raghavachari, A. Rendell, J. C. Burant, S. S. Iyengar, J. Tomasi, M. Cossi, N. Rega, J. M. Millam, M. Klene, J. E. Knox, J. B. Cross, V. Bakken, C. Adamo, J. Jaramillo, R. Gomperts, R. E. Stratma, O. Yazyev, A. J. Austin, R. Cammi, C. Pomelli, J. W. Ochterski, R. L. Martin, K. Morokuma, V. G. Zakrzewski, G. A. Voth, P. Salvador, J. J. Dannenberg, S. Dapprich, A. D. Daniels, O. Farkas, B. J. Foresman, J. V. Ortiz, J. Cioslowski and D. J. Fox, *Gaussian 09 Revision A.02*, Gaussian Inc., Wallingford CT, 2009.
55 A. D. Becke, *J. Chem. Phys.*, 1993, **93**, 5648–5652.
56 C. Lee, W. Yang and R. G. Parr, *Phys. Rev. B: Condens. Matter Mater. Phys.*, 1988, **37**, 785–789.
57 S. H. Vosko, L. Wilk and M. Nusair, *J. Phys.*, 1980, **58**, 1200–1211.
58 W. R. Wadt and P. J. Hay, *J. Chem. Phys.*, 1985, **82**, 284–298.
59 V. Barone and M. Cossi, *J. Phys. Chem. A*, 1998, **102**, 1995–2001.
60 M. Cossi, N. Rega, G. Scalmani and V. Barone, *J. Comput. Chem.*, 2003, **24**, 669–681.
61 H. X. Ting, R. Lu, P. Q. Xian, L. L. Xing, C. X. Peng, H. T. Chang, Y. B. Chun and Y. Z. Ying, *Eur. J. Org. Chem.*, 2006, 4014–4020.
62 C. Chen, D. H. Maldonado, D. Le Borgne, F. Alary, B. Lonetti, B. Heinrich, B. Donnio and K. I. Moineau-Chane Ching, *New J. Chem.*, 2016, **40**, 7326–7337.
63 Y. Wu, H. Guo, T. D. James and J. Zhao, *J. Org. Chem.*, 2011, **76**, 5685–5695.
64 S. Shome and S. P. Singh, *Chem. Commun.*, 2018, **54**, 7322–7325.
65 X. Chen, L. Hui, D. A. Foster and C. M. Drain, *Biochemistry*, 2004, **43**, 10918–10929.
66 F. E. Alemdaroglu, S. C. Alexander, D. Ji, D. K. Prusty, M. Borsch and A. Herrmann, *Macromolecules*, 2009, **42**, 6529–6536.
67 I. Hamachi, K. Yoshimura, A. Ojida, T. Sakamoto and M. Inoue, *F. Application, P. Data, P. Classification, U. S. 1 Cl*, US2009/0233373A1, 2009.